

https://dspace.org/

# Search for Wboson in the hadronic channel using the 2017 and 2018 Run-II data at ATLAS

**Mhlanga, Fortune Nhlanhla**

**2020**
https://hdl.handle.net/10539/31036

Downloaded from a DSpace repository. https://dspace.org/

# Search for W′ boson in the hadronic channel using the 2017 and 2018 Run-II data at ATLAS.



UNIVERSITY OF THE
WITWATERSRAND,
JOHANNESBURG

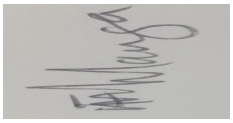
Fortune Nhlanhla Mhlanga
Faculty of Science, Department of Physics,
University of the Witwatersrand

*Supervisor*
Dr. Deepak Kar

In fulfilment of the requirement for the degree of
*Master of Science in Physics*
January 01, 2020

## DECLARATION

I, Fortune Nhlanhla Mhlanga, declare that this research report is my own, unaided work. It is being submitted for the degree of Master of Science in the field of Physics at the University of the Witwatersrand, Johannesburg. It has not been submitted for any degree or examination at any other university



September 21, 2020

# Abstract

The search for the hypothetical W′ boson that decays to the top-quarks and bottom-quarks is conducted using the full run 2 data, which was collected by the ATLAS detector at the Large Hadron Collider (LHC). This hypothetical W′ boson is reconstructed through its decay products. Hence, this study seek to improve the reconstruction of the top-quark by devising a method that selects top-quark jet candidates from large-radius jets (large-R jet) in an event. Several methods are tested to quantify which one selects more large-R jets that are true top-quark jets in a signal sample. Through this study a method that successfully selected more true top-quark jets was devised. The current simulated signal samples are generated using a Geant4 based full simulation, which needs a significant amount of resources to produce. The results that are obtained using the simplified fast simulation are tested if they are similar to the full simulation results, this is done by comparing the modelling of the large-radius jet substructure variables. This study shows that the fast simulation poorly models some of the large-R jet substructures variables.

# Acknowledgements

I would like to take this opportunity and acknowledge the following people who supported me throughout my Masters degree.

My greatest gratitude goes to my supervisor Dr. Deepak kar for allowing me to work with him, and for guiding me in this research project.

I would like to thank NRF for supporting me financially during this MSc degree, SA-CERN and Prof. Bruce Mellado for allowing me to visit CERN in-order to work with the experts and learn from them, and also to share ideas with other young scientists from different parts of the world.

I would also like to thank Dr. Debarati Roy, Dr. Josu Cantero Garcia, Dr. Hector De La Torre Perez, Dr. Aparajita Dattagupta and other ATLAS TopAnalysis group members for guiding me throughout the course of the research projects that we undertook together.

And finally, I would like to thank my friends and family for their unwavering support. Your encouragements and belief meant a lot to me.

# Contents

**Introduction** . . . . . 1

**1 The Standard Model of particles (SM)** **3**

1.1 The Higgs boson . . . . . 9

1.2 Success and limitations of the SM . . . . . 11

1.3 The W′ and Z′ in SM extensions . . . . . 12

**2 The ATLAS detector at the Large Hadron Collider** **13**

2.1 The Large Hadron Collider . . . . . 13

2.2 The ATLAS detector . . . . . 16

2.2.1 An overview of the coordinate system . . . . . 16

2.2.2 The tracking system . . . . . 18

2.2.3 Calorimeters . . . . . 20

2.2.4 The trigger system . . . . . 21

2.2.5 Data processing . . . . . 22

2.3 Jet reconstruction at ATLAS . . . . . 23

2.3.1 Jet algorithms . . . . . 24

2.3.2 Jet reconstruction . . . . . 25

2.4 Event simulation . . . . . 27

2.4.1 The full simulation . . . . . 30

2.4.2 The fast simulation . . . . . 31

**3 All hadronic W′ search** **34**

3.1 W′ decay models . . . . . 34

3.2 Large-R jets . . . . . 36

3.3 The comparison of the fast and full simulation distributions . . . 38

3.3.1 Large-R jet substructure variables . . . . . 38

3.3.2 Analysis strategy . . . . . 42

3.3.3 Results . . . . . 43

3.4 Summary of the fast and full simulation comparison . . . . . 48

3.5 Optimization of the top quark reconstruction . . . . . 50

3.5.1 Analysis approach . . . . . 51

3.5.2 Top-quark reconstruction methods . . . . . 51

3.5.3 The matching process . . . . . 53

3.6 Results . . . . . 54

3.7 Optimization of the top-quark reconstruction summary . . . . . 62

**4 Conclusions** **64**

**A Supporting distributions** **66**

**References** **88**

# List of Figures


1.1 The SM particles . . . . . 5

2.1 Shows the schematic diagram of the LHC . . . . . 15
2.2 Shows the overview of the ATLAS detector and its sub-detectors . 18
2.3 Shows the overview of the ATLAS inner detector . . . . . 19
2.4 Shows the calorimeter system of the ATLAS detector . . . . . 21
2.5 Shows the sketch of the ATLAS trigger system and its TDAQ system 22
2.6 This schematic diagram shows a detailed full simulation . . . . . 30

3.1 Shows the Feynman diagram . . . . . 35
3.2 The 1st splitting scale . . . . . 43
3.3 The 2nd splitting scale . . . . . 44
3.4 The large-R jet $\tau_{21}^{wta}$ variable . . . . . 45
3.5 The large-R jet $\tau_{32}^{wta}$ variable . . . . . 46
3.6 (a) Shows large-R jet ECF1 variable distributions that are modelled by the fast and full simulation. (b) Shows the large-R jet $p_T$ variable distributions modelled by fast and full simulation. . . . . 47
3.7 The large-R jet ECF2 . . . . . 48
3.8 The m_comb large-R jet $p_T$ matching fraction . . . . . 55
3.9 The m_comb large-R jet mass matching fraction . . . . . 56
3.10 The modified m_comb method for $\omega = 0$ mass matching fraction . 57

3.11 The modified m_comb method for $\omega = 0$ $p_T$ matching fraction . . 57
3.12 The modified m_comb method for $\omega = 1$ $p_T$ matching fraction . . 59
3.13 The modified m_comb method for $\omega = 1$ mass matching fraction . 59
3.14 Shows the probability of the selecting the top jet candidate . . . . 60
3.15 Shows the fraction of events that fulfill the DNN top tagger . . . 61
3.16 Shows the performance of all the methods . . . . . 61

A.1 (a) Shows the large-R jet $p_T$ variable from 0 to 500 GeV modelled by the fast and full simulation. (b) Shows the 1-point correlation function variable distributions under the large-R jet $p_T$ region of 0 to 500 GeV, it is modelled by the fast and full simulation. . . . . 66
A.2 Shows (a) the first splitting scale and (b) the second splitting scale variable distributions under the large-R jet $p_T$ region of 0 to 500 GeV, it is modelled by the fast and full simulation. . . . . 67
A.3 Shows for (a) the $\tau_{21}^{wta}$ and (b) the $\tau_{32}^{wta}$ variable distributions under the large-R jet $p_T$ region of 0 to 500 GeV, modelled by the fast and full simulation. . . . . 67
A.4 The large-R jet ECF2 . . . . . 68
A.5 (a) Shows the large-R jet $p_T$ variable from 500 to 1500 GeV modelled by the fast and full simulation. (b) Shows the 1-point correlation function variable distributions under the large-R jet $p_T$ region of 500 to 1500 GeV, it is modelled by the fast and full simulation. 69
A.6 Shows (a) the first splitting scale and (b) the second splitting scale variable distributions under the large-R jet $p_T$ region of 500 to 1500 GeV, it is modelled by the fast and full simulation. . . . . 70
A.7 Shows for (a) the $\tau_{21}^{wta}$ and (b) the $\tau_{32}^{wta}$ variable distributions under the large-R jet $p_T$ region of 500 to 1500 GeV, modelled by the fast and full simulation. . . . . 70

A.8 The large-R jet ECF2 . . . . . 71
A.9 (a) Shows the large-R jet $p_T$ variable from 1500 GeV and above modelled by the fast and full simulation. (b) Shows the 1-point correlation function variable distributions under the large-R jet $p_T$ region of 1500 GeV and above, it is modelled by the fast and full simulation. . . . . 72
A.10 Shows (a) the first splitting scale and (b) the second splitting scale variable distributions under the large-R jet $p_T$ region of 1500 GeV and above, modelled by the fast and full simulation. . . . . 73
A.11 Shows for (a) the $\tau_{21}^{wta}$ and (b) the $\tau_{32}^{wta}$ variable distributions under the large-R jet $p_T$ region of 1500 GeV and above, modelled by the fast and full simulation. . . . . 73
A.12 The large-R jet ECF2 . . . . . 74

# List of Tables

1.1 Shows the relation between symmetries and conservation laws [1]. 9

3.1 Shows the total matching fraction for all the examined W′ mass samples, when $\Delta = 0.15$. . . . . 54

3.2 Shows the total matching fraction for all the examined $W'$ mass samples for $\omega$ parameter equal to zero. . . . . 56

3.3 Shows the total matching fraction for all the examined W′ mass samples, when $\omega = 1$. . . . . 58

3.4 Shows the total matching fraction for all the examined W′ mass samples using the dnn top tagging. . . . . 60

# Introduction

Elementary particle physics is a subject that investigates the basic constituents of matter and how they interact with each other. The concept of particles such as the proton [2], neutron [3], and electron [4] was established by many experiments in the early 20th century. The discovery of new particles thereafter led to the introduction of the quark model [5], which describes a class of particles as the bound states of quarks and gluons.

The formulation of the Standard Model (SM) was a result of the theoretical successes and experimental observations, it provides the description of the fundamental particles and their interactions based on quantum field theory (QFT). The SM is considered a successful theory as many experimental measurements agree with its predictions.

The discovery of the Higgs boson [6],[7] in 2012 by the ATLAS (A Toroidal LHC Apparatus) and CMS (Compact Muon Solenoid) experiments at the LHC was the last piece of the SM that had been missing. Even though the discovery of the Higgs boson had completed the SM, the SM still falls short in explaining phenomenons such as dark matter, gravity, and neutrino mass. This has led to the development of a several extensions to the SM that seek to describe these unexplained phenomenons.

There are many theories that propose the physics beyond standard model. One class of these theories include the additional heavy gauge bosons. These new heavy gauge bosons that are predicted are usually called the $W'$ and the $Z'$ bosons (or W-prime and Z-prime bosons respectively) which have a similar decay modes to the gauge bosons of the standard model the W and the Z bosons. These newly proposed heavy gauge bosons are thought to be heavier than their standard model counterparts the W and Z bosons [8], [9], [10].

One of many experiments that probe the SM and beyond is the Large Hadron

Collider (LHC), which is located at CERN in the border of Switzerland, Geneva and France. Proton-proton collisions at high energies can produce an observable number of rare new particles, which can be searched for.

The studies that are presented by this thesis were all focussed on assessing the sensitivity of the W′ search. The results of these studies will be implemented on real data which was collected from the ATLAS detector.

The SM of particles is discussed in detail in chapter 1, chapter 2 describes the ATLAS detector and jet reconstruction, and chapter 3 presents the results of the studies and the last chapter is the conclusion.

# Chapter 1

# The Standard Model of particles (SM)

The description of all the elementary particles and their interaction in SM is depicted as quantum fields with degrees of freedom as many as the types and states of different particles. This explains why the same particles are indistinguishable as they are simply excitation of the same field [11].

Leptons, quarks, gauge bosons, gluons and the Higgs boson are the particles of the SM. These particles are usually represented by the Lorentz group and the internal symmetry group of the SM. The SM particles and its interactions can be represented by the SM Lagrangian which is stated as follows:

$$\mathcal{L} = -\frac{1}{4}F_{\mu\nu}F^{\mu\nu} + i\bar{\psi}\not{D}\psi + \psi_i y_{ij}\psi_j\phi + h.c + |D_\mu\phi|^2 - V(\phi). \tag{1.1}$$

Equation 1.1 shows the $\mathrm{SU}(3)_C \times \mathrm{SU}(2)_L \times \mathrm{U}(1)_Y$ symmetry terms. The $F_{\mu\nu}$ in the first is the electromagnetic field tensor, it also represents the field strength tensor of gluon fields in quantum chromodynamics (QCD). Following are the spinors ($\psi$) that represent the fermions and need the use of the gauge covariant

derivative D. The $\not{D}$ is the Feynman slashed notation which is used to show the contraction with a gamma matrix ($\gamma$). The $h.c$ term is the hermitian conjugate that needs to be included to take into account the anti-particles. The $y_{ij}$ is the Yukawa coupling which gives the chiral fermions mass. The scalar field $\psi$ is constructed using the covariant derivative, while the $V(\psi)$ the Higgs field potential is subtracted [12].

The $SU(3)_C$ group represents the strong force which acts on the colour charge C. The $SU(2)_L \times U(1)_Y$ group represents the electro-weak that acts on the weak hypercharge Y and the left-handed fermions (L) with a weak isospin $T_3 \neq 0$. This theory incorporates a variety of particles that are presented below [12].

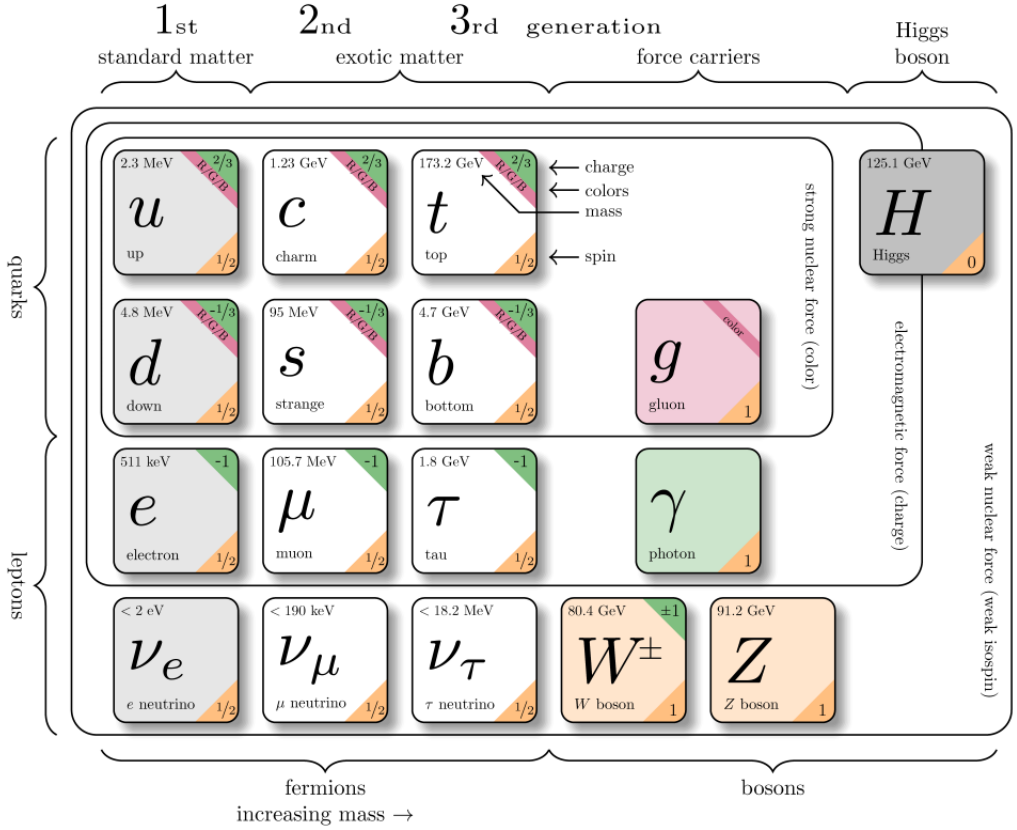



Figure 1.1: Shows the particles that are described by SM, with the first column, second column and the third column representing the first, second and third generation of particles respectively, which are all fermions. After the third column it is the bosons that are shown. The mass, charge, colour and spin of the particle is also shown in the respective particles. Adapted from [13]

All fermions have half-integer spin, while the bosons carry integer spins. Up to now, it is known that the basic constituents of matter are made up of fermions, which then interact with each other via exchange of gauge bosons. It is important to note that this exchange of gauge bosons can only occur to fermions that carry the same charge. In all interactions the charges are quantized and conserved, including coupling constants, they determine the strength of the interaction. The Higgs boson is the only known spin-0 scalar boson and all the massive SM particles interact with it [14].

**Fermions** All fermions have antiparticles, these antiparticles share a few properties with the fermions such as mass, but have opposite quantum numbers, although they also have half integer spins [11].
Fermionic group is made up of six quarks and six leptons as seen in Figure 1.1. The mass of fermions is the only difference between the particles in different generations. Fermions in higher generations can decay to fermions at lower generations, this implies that the particles in higher generations are unstable. Matter is made up of first generation particles [11].
The leptons are charged, and have a corresponding partner, the neutrino that is electrically neutral. In the first generation there is an electron ($e$) and its corresponding electron neutrino ($\nu_e$), in the second generation there is a muon ($\mu$) with its corresponding muon neutrino ($\nu_\mu$) and the third and last generation of leptons is the tau ($\tau$) also with its tau neutrino ($\nu_\tau$) [11].

The property that distinguishes quarks and leptons is the colour charge, leptons do not have any colour charge while the quarks do have the colour charge. This property of quarks has a consequence which will be seen in the upcoming chapters. The electrical charge of quarks is $+2/3$ and $-1/3$ which corresponds to the up-type and down-type quarks respectively, these types are found in each generation of quarks . In the first generation, there is up (u) quark with $+2/3$ electric charge and the down (d) quark with a $-1/3$ electric charge, the second generation consisted of the charm (c) and the strange (s) quark while in the third generation the top (t) and bottom (b) quark [11].

The weak isospin characterizes all the fermions, which is $\pm 1/2$ for all the left-handed fermions. The weak isospin doublet is for the charged leptons with their neutrinos in each generation. The zero weak isospin singlets describe all the right-

handed charged leptons, it is noticeable that the right-handed charged leptons are not coupled to neutrinos. The parity-violation of the weak interaction is introduced due to this singlets and doublets nature of leptons, which then implies that there is only couplings of the weak interactions and the left-handed fermions [11].

**Bosons** It was in the 1950s where the gauge theory was constructed to describe the interactions in the SM. The interaction between a force carrier and particle can be understood as force. The massless gauge bosons (Photons ($\gamma$)) are the force carriers in the quantum electrodynamic (QED) interactions. The interaction of relativistic particles through the electromagnetic force is explained by the QED [11].

Glashow, Salam, and Weinberg formulated a theory that unified the electromagnetic and the weak force into a single consistent theory [8],[15]. They managed to develop this theory based on the concepts of QED. The unified theory is founded on the combined symmetry group $\mathrm{SU}(2)_L \times \mathrm{U}(1)_Y$ [8],[15]. The single gauge boson that is denoted by B arises from the symmetry group $\mathrm{U}(1)_Y$. Generalizing the single electromagnetic gauge field $A^\mu$ are the three independent gauge fields ($\mathrm{W}^\mu = \mathrm{W}_1^\mu$, $\mathrm{W}_2^\mu$, $\mathrm{W}_3^\mu$) called the $\mathrm{SU}(2)_L$ gauge fields [16]. The basic electroweak interaction is given as:

$$-ig(J^i)^\mu W_\mu^i - i\frac{g'}{2}(j^Y)^\mu B_\mu \tag{1.2}$$

Where the vector fields $\mathrm{W}_\mu^i$ are coupled with strength $g$ to the weak isospin current $\mathrm{J}_\mu^i$, together with the single vector field $\mathrm{B}_\mu$ that is coupled to the weak hypercharge current $\mathrm{j}_\mu^i$ with the strength generally considered to be $\frac{g'}{2}$ [11].

The fields are given as $W^{\pm} = \sqrt{\frac{1}{2}}(W^1 \mp iW^2)$ with the mixing of

$$\begin{pmatrix} \gamma \\ Z \end{pmatrix} = \begin{pmatrix} cos\theta_W & sin\theta_W \\ -sin\theta_W & cos\theta_W \end{pmatrix} . \begin{pmatrix} B \\ W^3 \end{pmatrix} \tag{1.3}$$

where $\theta_W$ is the weak mixing Weinberg angle.
The strength of the electromagnetic interaction $e$ is related to the weak interaction strength $g$ through $e = gsin\theta_W$. The weak isospin $T_3$ and the weak hypercharge $Y$ determines the electric charge Q as follows:

$$Q = T_3 + \frac{Y}{2}, \tag{1.4}$$

From above, the photon that is described by the QED couples with the electric charge. The weak isospin couples with the two electrically charged bosons $W^{\pm}$. The Z boson couples to electric charge and the weak isospin with different strengths. The weak gauge bosons can interact with each other directly since they are themselves weakly charged. The photon can also interact with the $W^{\pm}$ since it is electrically charged. The $W^{\pm}$ boson has a mass of 80.4 GeV and the Z boson also has a mass of 90.2 GeV [11].

The Quantum Chromodynamics (QCD) [17] is the theory that describes the strong interaction. Eight massless gluons arise due to the symmetry group $SU(3)_C$, they couple with all particles that carry colour charge, this also mean that gluons can couple with each other. Red, blue, and green are the states that are used to denote the colour charge. The aforementioned colours do not relate to the colours that we use in our daily lives. The confinement and asymptotic freedom are phenomenon that are a consequence of the fact that gluons are massless and can couple with each other [11].

Confinement describes the fact that the quarks can not be observed in isolation, they can exclusively be observed in colour-neutral bound states such as baryons or mesons. The baryons contain three quarks and form a colour-neutral state, while mesons are made of one quark and its anti-quark to form a colour-neutral state [11].

This implies that the coupling strength of the strong interaction will tend to increase with increasing distance. It is concluded that coloured objects do not favour separation, to conserve colour charge. If they are being separated, energetically they generate new coloured particles until a colour-neutral state has been achieved. The asymptotic freedom describes that at small distances, the strong coupling is also small, while the coloured objects will behave as free objects with regards to the strong interaction [11].

## 1.1 The Higgs boson

Symmetry has an important role that they play in particle physics. From Noether's theorem all the theoretical symmetries have a conserved current associated with them [1]. Table 1.1 below shows a few examples of symmetries and their conserved quantities that appear in particle physics.

| Symmetry | Conservative law |
|---|---|
| Time translation | Energy |
| Space translation | Momentum |
| Rotation | Angular momentum |
| Gauge tranformation | Charge |

Table 1.1: Shows the relation between symmetries and conservation laws [1].

To give masses to the W and Z bosons the electroweak (EW) symmetry, the unification of electromagnetism and the weak force must be broken [18],[19]. The so-called Brout-Englert-Higgs mechanism is the simplest approach to introduce the spontaneous symmetry breaking, which is generally known as the Higgs mechanism. The single complex scalar field $\phi = |\phi|e^{i\theta}$ is the simplest model of the spontaneous U(1) symmetry breaking [11]. where its gauge-invariant potential field is described by $V(\phi) = \mu^2(\phi^\dagger\phi) + \lambda(\phi^\dagger\phi)^2 = \mu^2|\phi|^2 + \lambda|\phi|^4$. The continuous minimum of this potential is described by $|\phi|_{min} = \sqrt{\frac{-\mu^2}{2\lambda}} = \nu$, which is independent of the phase $\theta$. The choice of the angle $\theta$ by nature breaks the symmetry spontaneously. $\nu$ is the vacuum value or vacuum expectation value ($vev$) [20].

The potential of the vacuum state is $\phi = \frac{1}{\sqrt{2}} \begin{pmatrix} 0 \\ \nu \end{pmatrix}$ which breaks the $\mathrm{SU}(2)_L \times \mathrm{U}(1)_Y$ symmetry spontaneous of the electro-weak model. The field can be expanded in the radial direction with the parametrization

$$\phi = \frac{1}{\sqrt{2}} \begin{pmatrix} 0 \\ \nu + H(x) \end{pmatrix} \tag{1.5}$$

Where H is a physical scalar field, with its quantum excitations as the Higgs boson, with its mass term given as $m_H = \sqrt{2\mu}$ [20]. The Higgs boson generates masses for the W and the Z bosons as they couple to the Higgs field. Their masses are given as follows: $m_W = 0.5g\nu$, $m_Z = m_W/cos\theta_W$. The Higgs boson also provides fermion mass ($m_f$) that are consistent with the theory. The Yukawa couplings are used to generate the $m_f = y_f \frac{\nu}{\sqrt{2}}$ terms, where $y_f$ is a constant whose value is not predicted by the theory [11].

## 1.2 Success and limitations of the SM

The SM has been very successful ever since its inception. It predicted several particles, interaction, and rates with high precision. Some of the particles and interactions that have been observed completed all the three generations of particles and all the predicted interactions have also been observed. All the massive SM particles acquire their mass through their interaction with the Higgs boson [11].

Despite the successes of the SM, it is considered as an incomplete theory since it does not explain a number of the observations such as:

**Gravity:** The SM does not include gravity. Even though the gravitational interactions are very small but they are present in nature and a theory that does not include gravity cannot be considered complete [11].

**Dark Matter and Dark Energy:** There have been many astronomical observations that show that the ordinary matter and the energy content of the universe which is described by SM is about 5% [21], [22]. These observations also show that there is about 27% unknown kind of matter, which is referred to as dark matter. The rotation curves of galaxies show direct evidence of dark matter [23]. The so-called Dark Energy is a concept that is deducted from the remaining energy content of the universe. It is believed that the expansion of the universe is due to this energy [24].

**Matter-anti-matter asymmetry:** The SM postulates that matter and anti-matter should have been produced in almost equal amounts during the creation of the universe [25]. Although this conclusion is not in line with what we observe in the world, the only explanation this asymmetry in the world could be due to a possibility of regions in the universe where there is only domination of matter or anti-matter. This possibility is not supported by the recent research as it is not likely that these regions exist [26].

## 1.3 The W′ and Z′ in SM extensions

The incompleteness of the SM has led to some SM extensions that attempt to explain certain features of the universe that are not fully described by the SM. Several SM extensions include enhanced symmetries that predict these new heavy W′ or Z′ gauge bosons. These new heavy gauge bosons are considered to be the versions of SM W and Z bosons that are heavier. These gauge bosons are predicted to couple with the fermions in a way that is identical to SM W and Z bosons [27].There are a number of models that predict these new heavy gauge bosons such as the Sequential Standard Model (SSM)[27], Left-Right Symmetric Models (LRSM) [28],[29].

# Chapter 2

# The ATLAS detector at the Large Hadron Collider

## 2.1 The Large Hadron Collider

The Large Hadron Collider (LHC) [30] is a particle accelerator that lies in a circular tunnel with a circumference of about 27 km, 50-175 m underground. The LHC is located at the border of Switzerland and France. It is governed by the European Organization for Nuclear Research (CERN) which is based just outside Geneva, Switzerland. The LHC is constructed in the tunnels that were previously used for the Large Electron Positron (LEP) collider. There are two beam pipes at the LHC at which two beams of particles are injected into, in opposite directions in a vacuum. The particles that can be accelerated are heavy ions or protons [31]. At the interaction points, there are four detectors in the LHC: A Large Ion Collider Experiment (ALICE), A Toroidal LHC Apparatus (ATLAS) [32], Compact Muon Solenoid (CMS), and lastly the Large Hadron Collider beauty (LHCb). The physics studied by these experiments is different. ATLAS and CMS experiments investigates a variety of SM and beyond SM physics. The primary objective

of the LHCb experiment is to investigate the b-quark physics and the Charge Parity (CP) violation. The ALICE experiment is designed to investigate the quark-gluon plasma through heavy-ion collisions [33].

**Energy of the Beam** The linear acceleration of the LHC is provided by eight superconducting radio-frequency cavities, while the 1232 superconducting dipole magnets maintain the circular path of the beam. About 8.3 T of the magnetic field is generated by the dipole magnets, with the liquid helium at 1.9 K used for cooling the niobium-titanium wires that are used. The additional 392 quadrupole magnets focus the beams. The beam pipes intersect at four points [31].
For particles to reach the maximum energy of the LHC there are several stages of acceleration that are needed. The CERN accelerator complex is shown by Fig.2.1. The LINAC 2 linear accelerator is the protons that are initially produced through ionization of the hydrogen, to the energy of 50 MeV. From the LINAC 2, these protons are injected to the Proton Synchrotron Booster (PSB) then accelerated to about 1.4 GeV of energy, then passed to the Proton Synchroton (PS) to be accelerated to an energy of about 25 GeV, then they are accelerated to the energy of 450 GeV by the Super Proton Synchrotron (SPS). Particles from SPS are finally injected to the LHC ring that continues to accelerate them to the beam energy of 6.5 TeV [33].

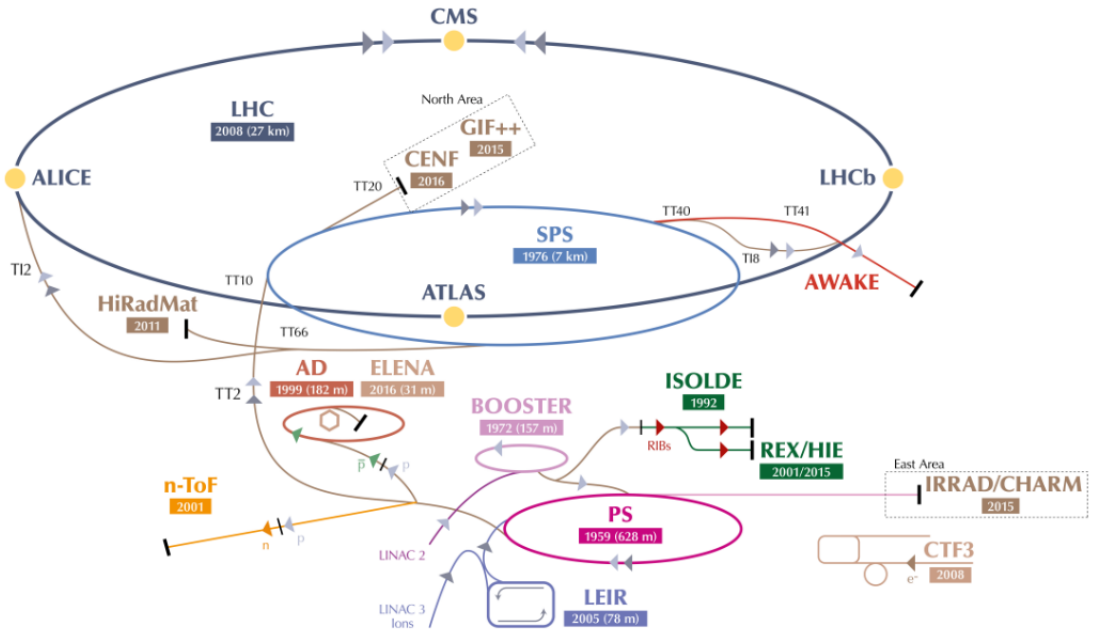



Figure 2.1: Shows the schematic diagram of the LHC, adapted from [34]

**Luminosity** The instantaneous Luminosity $\mathcal{L}$ is another important parameter apart from the beam energy. The $\mathcal{L}$ is related to the rate of collisions $R$ as follows: $R = \sigma\mathcal{L}$, with $\sigma$ as the cross-section of the proton-proton collisions. The $\mathcal{L}$ is defined as follows:

$$\mathcal{L} = \frac{n_p^2 n_b f}{4\pi\sigma_x\sigma_y}, \tag{2.1}$$

$n_p$ represents the number of protons per bunch, a number of bunches are represented by $n_b$, $f$ is the revolution frequency, while the spreading of the beam in the beam transverse plane at the interaction points is represented by $\sigma_x$ and $\sigma_y$. The amount of collisions produced by the LHC or which is recorded by an experiment is usually represented by the integral of $\mathcal{L}$ for a certain period of time [31].

## 2.2 The ATLAS detector

The ATLAS detector is built in one of the four interactions points of the LHC, it serves as a multiple-purpose particle detector. The ATLAS detector is designed such that it is symmetric about the direction of the beam. It is made up of the inner tracking detector, the thin superconducting solenoid that is surrounding it, the electromagnetic and hadronic calorimeters, and the three large superconducting toroidal magnet systems that incorporate the muon spectrometer [31].

### 2.2.1 An overview of the coordinate system

The nominal interaction point is the origin of the ATLAS coordinate system, with z-axis defined along the beam direction, and the transverse to the beam direction defines the x-y plane [32]. In spherical coordinates it is mapped as follows: the azimuthal angle $\phi$ is defined on the transverse plane that is identified by x-y plane, at the range of -$\pi$ to $\pi$. The quantity measured from the z-axis is the polar angle $\theta$ but is generally expressed in terms of the pseudorapidity

$$\eta = -ln(tan(\theta/2)). \tag{2.2}$$

Pseudorapidity of a massless particle is equal equivalent to rapidity which is defined as

$$y = \frac{1}{2}ln(\frac{E + p_z}{E - p_z}), \tag{2.3}$$

rapidity is also used for massless particles such as photons. In the rapidity definition, E is the energy of the particle and its longitudinal momentum is represented by $p_z$. Rapidity is invariant under Lorentz boosts, while the polar $\theta$ is not [31].

To measure the distance between two four-vectors in the $\eta$ - $\phi$ plane is done by

the $\Delta R$ variable which is calculated as

$$\Delta R = \sqrt{\Delta\eta^2 + \Delta\phi^2}. \tag{2.4}$$

The transverse momentum ($p_T$) of the particle is calculated as

$$p_T = \sqrt{p_x^2 + p_y^2}, \tag{2.5}$$

which is the projection of the particle's momentum vector in the transverse plane. The transverse energy of the particle is calculated as

$$E_T^2 = p_T^2 + m^2, \tag{2.6}$$

where $E_T$ is transverse energy. At the first approximation, the momentum of the incoming parton is only directed along the z-axis, that implies that the transverse momenta of the outgoing particles must add up to zero unless there are some particles that are not detected by the detector [31]. The quantity

$$|\vec{P}^{miss}| = -\sum_i \vec{P}_{T,i}, \tag{2.7}$$

is called the missing transverse momentum, it can be used to estimate the vector sum of transverse momenta of undetected particles. The missing transverse energy is defined as $E_T^{miss} = |\vec{P}^{miss}|$ [31].

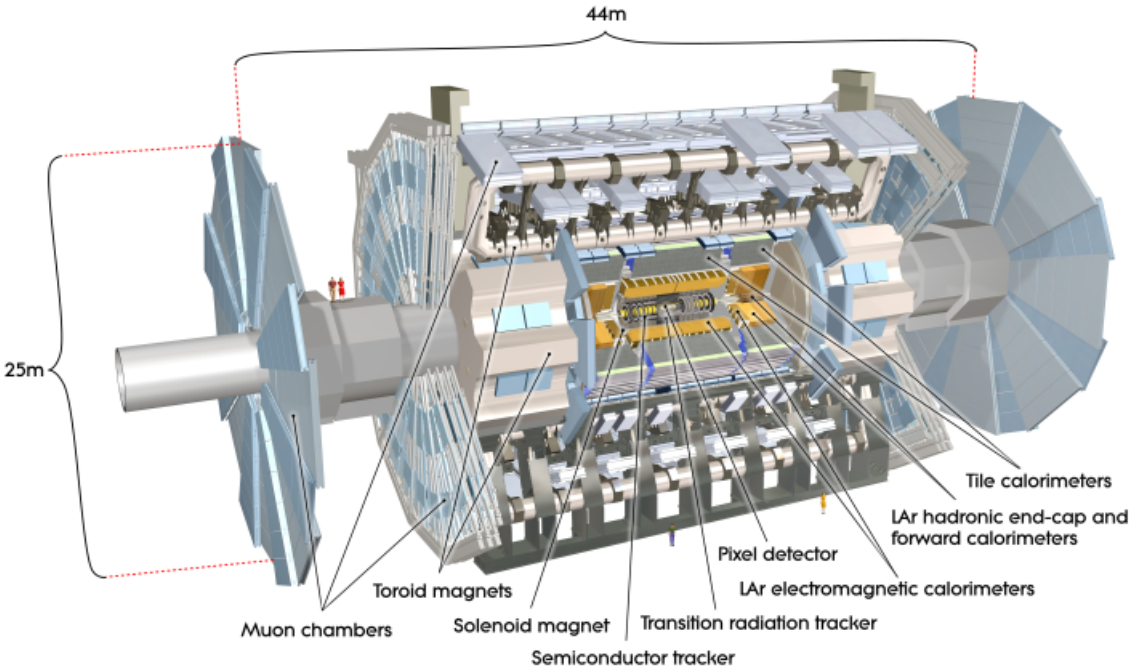



Figure 2.2: Shows the overview of the ATLAS detector and its sub-detectors, which in total weighs 7000 tonnes, adapted from [32]

### 2.2.2 The tracking system

To attain good momentum and vertex resolution, the tracking detector needs to have a fine granularity. These features are offered by the pixel and silicon micro-strip (SCT) trackers that work with the straw tubes of the Transition Radiation Tracker (TRT). The tracker measures the curved trajectories of the charged particles such that their momenta can be determined [32]. The ID layout is shown by Figure 2.3 below.

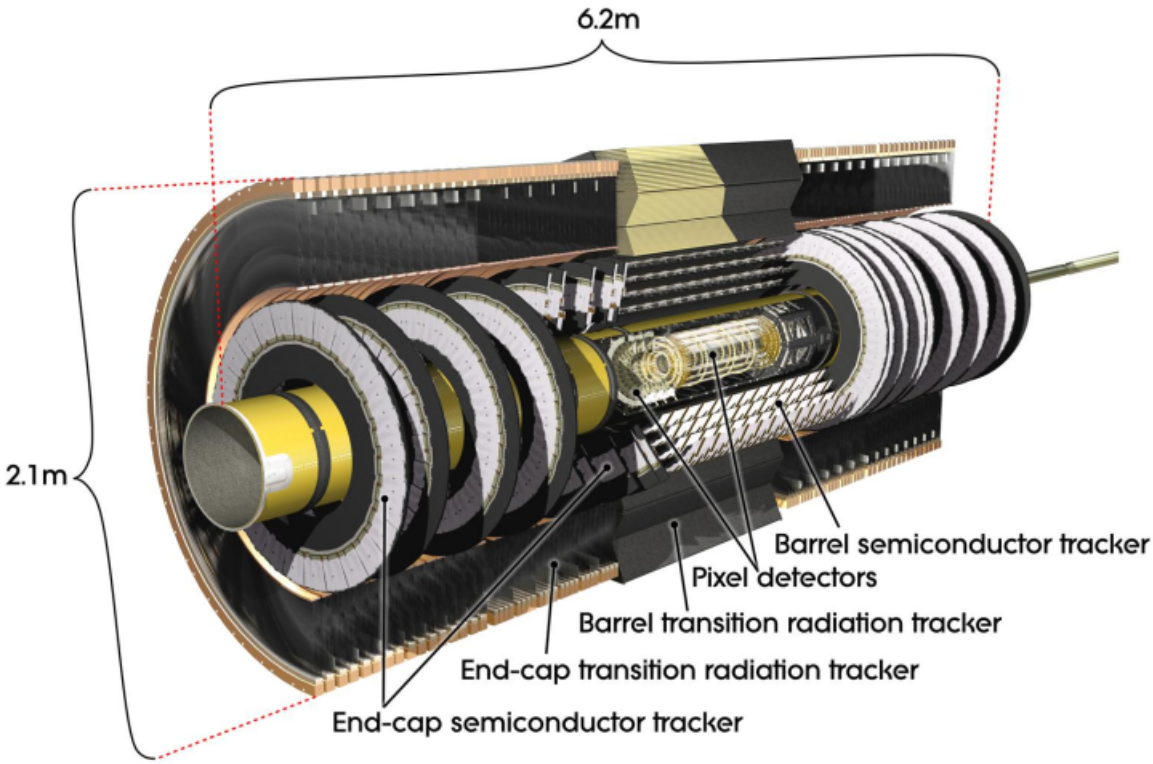



Figure 2.3: Shows the overview of the ATLAS inner detector, adapted from [32]

A magnetic field of 2 T which is generated by the central solenoid surrounds the ID, it extends to a length of about 5.3 m in a diameter of 2.5 m. About $|\eta| < 2.5$ region is covered by the precision tracking detectors, the pixels and the SCT. They can be found in the barrel region where they are arranged on concentric cylinders around the beam axis, in the end-cap regions they are found on disks that are perpendicular to the beam axis. The silicon pixel detectors are used to achieve the highest granularity around the vertex region. The three-pixel layers crossed by each track are segmented in the $R - \phi$ and $z$ coordinates. The pixel sensors have a minimum size of $50{\times}400$ $\mu$m$^2$ in the $R - \phi \times z$. In the barrel, there are intrinsic accuracies of $10\mu$m in $R - \phi$ and 115 $\mu$m in the z-axis, while the disks and the intrinsic sensors are $10\mu$m in $R - \phi$ [32].

### 2.2.3 Calorimeters

The electromagnetic (EM) and hadronic calorimeters measure the energy of all the particles that are produced in a collision event, apart from the muons and neutrinos. Figure 2.4 shows the calorimeters as they span $|\eta| < 4.9$ region. The calorimeters use several techniques that are suited for the different physics processes and for the radiation environment over this $\eta$ range. For the $\eta$ region that matches the inner detector, the precision measurements of electrons and photons suit the fine granularity of the EM calorimeter. The rest of the calorimeter's coarser granularity is enough to satisfy the physics requirements for the jet reconstruction and the $E_T^{miss}$ measurements [32].

This makes the depth of the calorimeter an important design consideration. The EM calorimeter has a total thickness that is greater than 22 radiation lengths ($X_o$) in the barrel and a thickness that is greater than 24 $X_o$ in the end-caps. A good resolution for high-energy jets is provided by the approximate 9.7 interaction lengths ($\lambda$) of the calorimeter in the barrel.

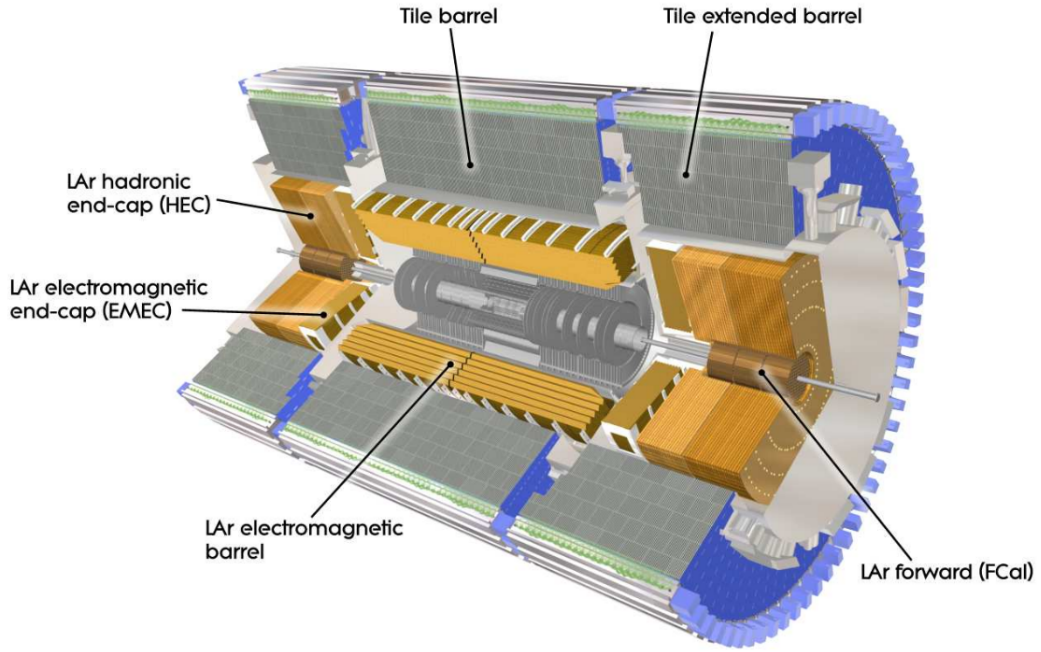



Figure 2.4: Shows the calorimeter system of the ATLAS detector with its essential components, adapted from [32]

### 2.2.4 The trigger system

The LHC has the instantaneous luminosity of $10^{34}$ cm$^{-2}$s$^{-1}$ with a bunch spacing 25 ns, this result to an average number of interactions to be about 23 per bunch-crossing, this corresponds to $10^9$ interactions per second. Hence there is a need to use a triggering system that is selective. The main objective of the Trigger and Data Acquisition (TDAQ) system [32] is to decrease this rate to be $\sim$1 kHz, this is achieved by storing data that result from high energy events that are considered to be rare as these events may contain interesting physics. In Run-II, the trigger system was operated using an online two trigger systems that were tied together, the trigger system consisted of the Level 1 (L1) and the Higher Level Trigger (HLT), the events stored had to meet demanding criteria in the trigger system. The first level trigger (L1) is hardware-based, it depends on the calorimeters (Calo) and the muon spectrometer (Muon) to determine interesting

physics events, as shown by Figure 2.5. The TDAQ manages the flow of data in the online tiers, all the events that meet the minimum requirements are then passed into data streams that cater for offline physics analysis, the trigger level analysis and the detector calibration. It is at this point where all the objects that do not meet the requirements are discarded completely. The computing infrastructure is used in order to reconstruct the data from the streams into information that can be used.

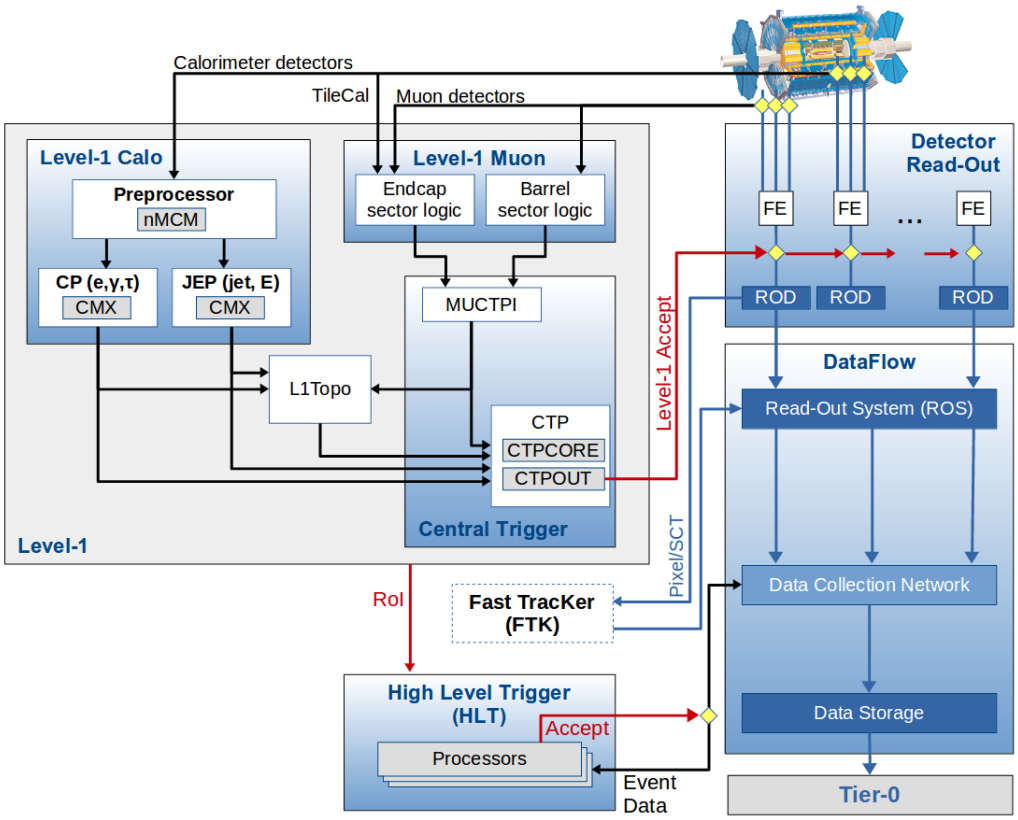



Figure 2.5: Shows the sketch of the ATLAS trigger system and its TDAQ system, adapted from [35]

### 2.2.5 Data processing

At the CERN computing facility, it is where the data that is recorded from the ATLAS detector is sent to. The Event Summary Data (ESD) format is

encoded from the raw data after being processed. It is then that these files will be sent to the LHC computing Grid [32], which is a cluster of computers that is in the world-wide network. These ESD files are processed further and broken into smaller Analysis Object Data files (xAOD), these files help to keep information depending on the individual analysis as to which specific physics objects are important. A large fraction of the information of an event is kept in the xAOD for data and simulated events. Generally, the xAOD datasets of simulated events are as large as tens of TB. There is a need for a reduction step which is called derivation which is performed by large analysis groups. The resulting files from the derivation are processed by individual analysers to ROOT [36] ntuples which can be handled by any personal computer that has a Root analysis framework [31].

## 2.3 Jet reconstruction at ATLAS

Detector signals are processed into useful physics objects such as the electrons, photons, muons, jets, tracks and missing transverse momentum before they are used by any physics analysis. This analysis uses only jets, hence their reconstruction will be described.

The formation of hadrons from quarks and gluons is called hadronisation. This process is due to the QCD colour confinement which plays a role at low energy scales, this forces the soft partons that evolved to hadronise (with the exception to the top-quark since it decays quickly). In parton showers this process of hadronization is non-pertubative.

A spray of collimated particles that result from high energy quarks and gluons are called jets [37]. Quarks and gluons originating from hard-scattering can produce gluons that split into a quark-antiquark pair. During the hadronization process

stage, the colour neutral hadrons are produced.

### 2.3.1 Jet algorithms

An algorithm that defines a jet must satisfy a several criteria. The definition of a jet must not depend on the order of perturbation theory calculations and must be able to produce a finite cross-section at any order of a given perturbation theory. This implies that the jet definition has to be infrared and collinear safe (IRC), this means that the set of hard jets that are created in an event are not changed by the any collinear splitting or the addition of a soft emission.
The current jet definitions at LHC are based on the sequential recombination algorithm class, which clusters particles by using a distance metric $d_{ij}$ and $d_{iB}$, to be defined below. Given a final-state pair of particles $i$ and $j$, the metric distance $d_{ij}$ will be the distance between the pairs and $d_{iB}$ is the distance to the beam. The sequential recombination algorithm operates in the following way:

- Find the smallest value amongst all the possible $d_{ij}$ and $d_{iB}$.
- If the smallest value is $d_{ij}$ then $i$ and $j$ are merged together.
- If the smallest value is $d_{iB}$ that means the corresponding cluster or input is a jet.
- The algorithm stops once all the inputs have been categorised.

The metric distance is defined as:

$$d_{ij} = min(p_{T,i}^{2p}, p_{T,j}^{2p}) \frac{\Delta R_{ij}^2}{R^2}, \tag{2.8}$$

The distance to the beam is defined as:

$$d_{iB} = p_{T,i}^{2p}, \tag{2.9}$$

from Equation 2.8, R is a fixed parameter which corresponds to the jet radius, $\Delta R_{ij}$ is the angular distance between the particles, and the type of the algorithm is determined by the value of $p$. When $p = 1$, the algorithm clusters soft particles together first, this algorithm is called the $k_t$ algorithm. For $p = 0$, the Cambridge-Aachen algorithm clusters the particles by using only the angular distance. Lastly, when $p = -1$ we have the anti-$k_t$ algorithm which clusters the hard radiation first. The anti-$k_t$ is the one that is commonly used, this is because it creates jets are relatively circular, which make it easier for calibration in the experiments [38].

### 2.3.2 Jet reconstruction

To perform jet reconstruction at ATLAS there are three general stages: the first stage is to define the four-vectors which are the inputs, then follows the definition of the jet algorithm and the parameters, and finally the calibration of a jet.
Topo-clusters are used for jet reconstruction as inputs, these are calorimeter cells which are topologically-grouped noise-suppressed clusters. The seed cell(s) with at least $4\sigma$ of energy from the topo-clusters, with $\sigma$, is the average amount of noise that is expected in the cell concerned, which is the sum of all the expected electronic and pile-up noise [39]. All the cells that have at-least $2\sigma$ and adjacent to the three-dimension seed cell(s) are grouped together, this is done until there are no more cells adjacent to the seed cell(s). The process is concluded by adding all the calorimeter cells that are adjacent to the topo-cluster [40].
The energy of isolated topo-cluster results from summing the energies of its constituents. Topo-clusters calibration can occur at raw (electromagnetic, EM) scale, where the energy of an isolated topo-cluster is equivalent to the total energies of its constituent cells, or be calibrated to the local cell weighting (LCW) scale [40]. The advantage of using the LCW scale is that it considers the difference between the electromagnetic and the hadronic interactions that are found in the ATLAS

calorimeters, by doing so, the LCW is able to correct the average topo-cluster to the hadronic energy scale.

The jet reconstruction algorithms are applied once the jet inputs have been formed. At ATLAS, jets are generally created by using the anti-$k_t$ algorithm, usually with the radius parameter (R) of 0.4 or 1.0, where R is equal to 0.4 the jet is called the small-radius jet (small-R jet) while for R is equal to 1.0 the resulting jet is called large-radius jet (large-R jet). Since small-R jets capture most of the energy from the shower which corresponds to a single parton, it is usually preferred by most physics analyses.

In a simulation, it is preferred that there must be a close correlation between the reconstructed level information and the truth level information. The differences that are usually observed between the reconstructed jets and the energy scale that corresponds to the truth jet are due to some effects such as the pile-up. To resolve these differences a multi-stage calibration process is employed such that the reconstructed jets and the truth jets can be closer to each other.

The LHC has a high instantaneous luminosity that results in high rates of multiple proton-proton interactions that occur simultaneously in a single bunch crossing, this phenomenon is called pile-up [41]. Correcting the pile-up effects are the first steps in the calibration process. The energy scale of the jet is increased by the pile-up in each event. In order to calibrate a jet that is in a low-pile-up event and the one that is in a high-pile-up event, it is important to subtract this pile-up energy meaningfully to allow the calibration process to occur.

Even after the application of pile-up reduction, from the calibrated jet response there remains some pile-up dependence. Two residual corrections are applied to correct the remaining effects of pile-up. It is observed that the jet response linearly depends in both the number of reconstructed primary vertices ($N_{PV}$) and the mean number of extra proton-proton collisions in a bunch crossing ($\mu$). The

$p_T$ that is pile-up corrected is expressed as follows:

$$p_T^{corr} = p_T^{reco} - \rho \times A - \alpha \times (N_{PV} - 1) - \beta \times \mu, \tag{2.10}$$

With $\alpha$ and $\beta$ determined via a several $\eta$ region linear fits, A is the area of a jet and $\rho$ is the median $p_T$ density of jets in the $\eta - \phi$ plane.

To bring the reconstructed jet energy closer to the truth energy scale a calibration is derived after the application of the pile-up correction. The matching of the reconstructed jets to the truth jets if $\Delta R < 0.3$ is performed in order to derive this calibration. To avoid nearby effects this is done on the isolated truth jets. The numerical inversion method [42] is used to calibrate the jet energy scale. It is then that these calibration factors are applied to all the jets. A global sequential calibration is derived after the Monte-Carlo calibration have been applied, this is done to account for any differences in the jet composition and the energy distribution coming from the calorimeter response.

The last step in the jet calibration is to correct the differences in the jet response in the data and the Monte-Carlo, they can possibly be caused by imperfections in the detector description, imperfect detector response modelling, or any simulation of the hard-scatter differences. Usually, the $p_T$ of a jet is compared to a well-measured reference object, this is done to measure the differences [42].

## 2.4 Event simulation

Event generation is the first step in the ATLAS [43] simulation software. The process of producing complete events that begin from proton-proton initial states is the general purpose of event generators. For event generation, a generator can used alone or with other generators that are specialised to better describe certain final states. The event generators have many parameters and some of them are

co-related. Some of these related parameters are the QCD coupling constant and electro-weak parameters, others are also used to give a description of models that parametrizes the long-range forces of QCD, soft QCD, and electro-weak processes [44].

The event generation at ATLAS runs within the Athena Framework. The event information is transferred from the interfaces into the object format that is usable by the ATLAS software. These events are stored as HepMC [45] POOL files. There are a number of event generators that are used at ATLAS, the ones that are commonly used for large-scale production are PYTHIA [46], HERWIG [47] [48] [49] , Sherpa [50], and MC@NLO [51]. To deal with the B-decays especially where the physics is sensitive to the decays of B hadrons the EvtGen [52] is usually used. The production of vector boson scattering events is done by MadGraph [53].

If the particles have the proper life time ($\tau$) multiplied by the speed of light ($c$) is above 10 mm they are considered to be stable, otherwise, they are considered unstable by the event generators. A stable particle can propagate a reasonable distance such that they can have an interaction with the detector material before they can decay [44].

At generation time only events with certain characteristics are kept, these properties could be the presence of certain number of leptons or jets, with specified $p_T$ thresholds [44].

Simulations help us to study how the ATLAS detector responds to a wide range of physics processes and scenarios, event generators produce events at the particle level, in order to compare it to data it must be passed into detector simulation [44]. The simulation programs have been integrated into the ATLAS software framework [54].

In general, the simulation software chain is partitioned into three steps which can

be merged into a single job. These steps are as follows: event generation and the immediate decays, physics and detector response, and digitization. This energy is recorded as "hits", which contains the total energy deposition, location, and time, and they are written to the output file which is called the hit file [44]. The simulation output can be presented in a way that is an object-based format or in a way that is similar to the ATLAS data acquisition system (DAQ) output. The data from the ATLAS detector and the simulation is run through the same ATLAS trigger and reconstruction packages [44].

To model the complex detector geometry and physics description, large computing resources are needed in the standard ATLAS detector simulation. This demand of the large computing resources has led to the construction of several varieties of fast simulation [44].

The simulation of the physics events includes the simulation of the detector response in detail, these events are essential to all the high-energy physics experimental analysis [55]. This task requires elementary physics processes to be described precisely as well as the simulation of the interactions of particles using the in-depth models of the detection apparatus [55]. The signatures of potential new physics have very small cross-sections compared to the background processes [55].

The detector simulation models the interactions of particles as they pass through the detector material and then studying the energy deposited by these particles in the material [56]. There is a large amount of computing time that is specifically reserved for the particle interaction simulation using the active and passive detector material and determining the detector response [55].

The simulation of each event at ATLAS can take several minutes, hence this step is considered to be the slowest. Normally the simulation jobs are divided into groups of 50 or fewer events and not all of them are completed in a single simu-

lation job [44].

The simulation output file consists of the record of all the particles that are produced by the generator and the same particles after they have interacted with the detector. Besides there is a truth information, which is the record of all the particles that are produced by the generator. Using the truth information, the Simulated Data Objects (SDO) are created in the digitization jobs. These SDOs are responsible of mapping the hits in the sensitive areas of the detector to the particles that are in the simulation truth information. The truth information is very useful especially in the simulation studies that measures the performance of a reconstruction software [44].

### 2.4.1 The full simulation

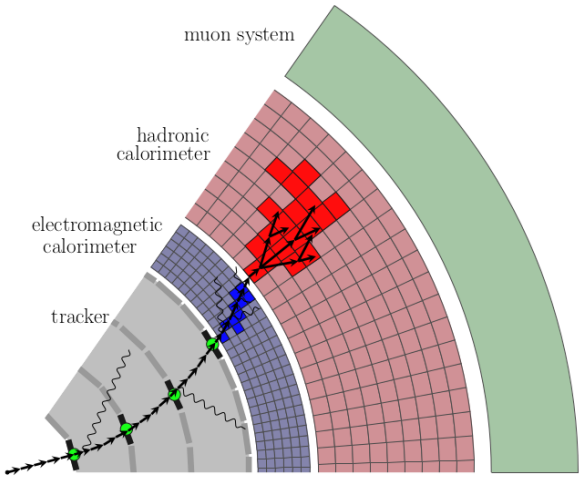



Figure 2.6: This schematic diagram shows a detailed full simulation, where a particle is followed in a step-by-step and its energy deposits is recorded in the sensitive parts of the ATLAS detector as it transverses through [57].

At ATLAS the GEANT4 [58] simulation toolkit known as a full simulation is used to mimic how the particles behave as they travel through the material of the detector [57]. Full simulation models the ATLAS detector precisely [55], this

requires significant central processing unit (CPU) time [55].

The simulation takes in a set of particles, a proposed structure of physics processes that may be encountered by particles and the geometry description. Geometry description includes details on which parts of the detector are sensitive to the particle passage, this implies that during the particle-matter interaction in the sensitive volume a signal is produced. A step-by-step process is shown by Figure 2.6. All the defined processes are considered, the passage of secondary particles is created, the deposited energy of the particles that transverse a sensitive material is saved so that it can be passed to the digitization and reconstruction algorithms. The information of the parts at which the detector is sensitive to the passage of these particles is also included, this implies that when there is a particle-matter interaction a signal is produced at the sensitive volume [57].

### 2.4.2 The fast simulation

Full simulation is used for the complicated detector geometry and detailed physics description. To achieve the ever-increasing statistics for many physics studies, there is a need to use a faster simulation than the currently used full simulation. The development of fast simulation programs is done to complement the full simulation, such that it can be used in physics analyses that do not require the detailed ATLAS simulation [44].

Full simulation spends most of its simulation time simulating the particles that move through the calorimetry. The Fast G4 Simulation is designed to accelerate the slowest areas of the full simulation [59]. The Fast G4 simulation aims to remove all the low energy electromagnetic particle from the calorimeter and then replace them with pre-simulated showers that are stored in memory. In this way, the Central Processing Unit (CPU) time is reduced by a factor of three in the hard scattering such as $t\bar{t}$ production, with very minimal effects to the results

[44].

The ATLFAST-II is developed to supplement full simulation studies. This fast simulation program simulates events as quickly as possible but still able to run the standard ATLAS object reconstruction. The ATLFAST-II is constructed with two components: the Fast ATLAS Tracking Simulation (Fatras) for inner detector and muon system simulation [60] and the Fast Calorimeter Simulation (FastCaloSim) is used for calorimeter simulation [44].

The FastCaloSim package provides a parameterized simulation of the particle energy response, and the ATLAS calorimeter's energy distribution to reduce the calorimeter simulation time in such a way that an event takes only a few seconds to be simulated [61].

The fast simulation reduces the CPU consumption in the following ways:

- It uses the reconstruction geometry of the calorimeter which describes the calorimeter cells as cuboids in $\eta$, $\phi$ and the calorimeter depth, where the forward calorimeter cells are cuboids in x,y,z. This assumption is acceptable for regions of the electromagnetic calorimeter that are homogeneous, but only to approximate other calorimeters [61].

- The fast simulation also uses parametrization to develop particle showers in the calorimeter. It averages the lateral shower properties and the uncorrelated lateral energy fluctuations to reproduce the longitudinal shower properties that include fluctuations and correlations [61].

- The photons, electrons and charged pions are the only particles that are parametrized, while the charged pions are utilized for all hadrons [61].

The use of fast simulation approach attempts not to simulate the particle's path through matter step-by-step but parametrizes the overall response of the sub-

divisions of the detector. The product of this simulation is that it reduces the most time-consuming part of the simulation which is the electromagnetic shower development in the calorimeters. The parametric approach that is hugely used in the fast simulation is also used to replace all the simulation, digitization, and reconstruction. This parameterization takes into consideration of all the physics effects which can be encountered by the particle in the tracker, performance of the detector, and the procedures of reconstruction [57]. The idea of the fast simulation has been accepted because more often for data analysis, the accuracy of the full simulation is not required [57]. The use of fast simulation reduces the precision of the results in the gain of speed.

# Chapter 3

# All hadronic W′ search

## 3.1 W′ decay models

This thesis focuses on the search for the W′ boson in the fully hadronic channel. The W′ boson is a hypothetical mediator of the new charged vector current which is massive, such that it can decay to a number of particles. The W′ boson is predicted by many beyond Standard Model (SM) theories, it has spin 1 with $\pm$ 1 as its electric charge. At the hadron colliders, the W′ boson can be detected via the production of fermions.

The decay of the W′ $\rightarrow \ell\nu$ is the most commonly studied channel, where the $\ell$ is the lepton, which can be an electron or muon. Events with high $p_T$ lepton and the significant $E_T^{miss}$ are used. The presence of a neutrino ($\nu$) is usually deduced from these observables, as it escapes the hadron colliders without detection [62]. The Left-Right Symmetry Models (LRSM) [29],[63],[28] also predict the right handed W′ ($W'_R$) with a very large mass compared to a right handed neutrino ($N_R$) which it decays to, and a lepton [64].

The W′ can also be massive enough to decay to anti-top and bottom quarks ($\bar{t}$b) or top and anti-bottom quark (t$\bar{b}$), generally this channel is called $tb$ at ATLAS.

This decay channel provides an opportunity to investigate the fully hadronic decay of the W′ (W′ → $tb \to bbq\bar{q}$, where $q$ and $\bar{q}$ are light quarks) as shown by Figure 3.1. The W′ → $tb$ does produce leptons, the studies in the leptonic and fully hadronic channel are done separately.

Another possible decay is that of the W′ → $tb \to bb\ell\nu$ channel. This is one of many decay channels that permits the W′ boson to be reconstructed fully [65].

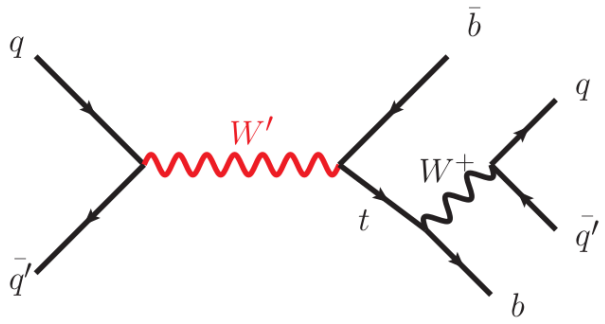



Figure 3.1: Shows the Feynman diagram, where the W′ decays to the bottom and top quark which further decays to a bottom quark and the SM W boson which further decays to light quarks [66].

The hadronic final state decays that result from high $p_T$ particles such as the W bosons, Higgs bosons, top quarks and probably new particles such as W′ and Z′ [67], are likely to be collimated into a single jet that is characterised by very distinct substructure and large mass [68]. Jet substructures depict the internal features of the hadronic jets, which carry information that is used to identify the decays of heavy particles [69]. The jet substructure is used as a tool to study the radiation pattern inside the jets, its techniques have improved the sensitivity for physics searches [70]. The use of the jet substructure at LHC has inspired a lot of new theoretical ideas and new reconstruction techniques to investigate untouched exciting regimes [70].

## 3.2 Large-R jets

Reconstruction of jets requires jet algorithms, these are well-defined procedures to collect detector tracks, and calorimeter cells converted to jet four-momenta, the reconstruction of jets is well described in Chapter 2. The anti-$k_t$ algorithm [71] is used in the reconstruction of large-R jets that are used in this thesis. The anti-$k_t$ algorithm is a sequential-recombination algorithm that produces conical jets.

As higher energies are probed: heavy particles that have transverse momentum larger than their masses ($p_T >> m$) are produced in large quantities, these particles are referred to as boosted objects.

The large-R jets used for this study contains the decay products of the top quark ($t \rightarrow Wb$) that arise from the high-mass resonances such as W$'$ and Z$'$. These large-R jets are used as a proxy for the top quark. Generally, a jet with large radius would encompass the boosted top quarks decay products. The large-R jets that are used in this study have a jet radius of 1.0, small-R jets with jet radius of 0.4 as the subjets that are enclosed by the large-R jet.

Light quark jets generally form the background to the top quark decays signal. In boosted regimes, the background may gain mass via radiation, that could be in the same range as of the heavy particles. Separating between the signal jets (these are jets that results from the top quarks for this thesis) and background jets becomes challenging. Attempts to resolve this challenge have led to the development of jet substructure techniques that probes the internal dynamics of jets.

Typically, the detector captures more than final states that come from hard scattering events. Multiple parton interactions (MI) and event pileup would generally contaminate the final state. The total effect is that hadrons arising from MI, pileup or other radiations would spatially protrude with hadrons that come from final state radiation (FSR), this further complicates the procedure of finding a

jet. Hence, there is need to look for a jet that is sufficiently large to encompass all the hard scattering decay products and consider a broad angle of FSR emissions. Identifying and removing contamination from each jet is the idea that originates from observation that there is normally one hard scattering in each event, and the rest of the remaining sources of radiation are potentially much softer. Hence, inspecting inside a jet and getting rid of any soft radiation via subjets or other techniques improves jet reconstruction [72].

At ATLAS all the large-R jets are trimmed, this method determines the regions of a jet where there is the most energy and the constituents that are outside this region are then groomed away, in order to clean the soft contamination to the jets. This is done by re-clustering the constituents of a large-R jet into subjets that have $R_{sub} < R_{jet}$ by using the $k_t$ algorithm, while discarding any subjet with $p_T < f_{cut} \times p_{T,jet}^{ungroomed}$, where the $f_{cut}$ is a dimensionless parameter that is fixed and $p_{T,jet}^{ungroomed}$ is the $p_T$ of the original jet. The $k_t$ algorithm is preferred for clustering subjets. This is because the anti-$k_t$ algorithm clusters radiation from hardest to softest, it also creates imbalanced subjets by assigning nearly all the energy to a single subjet. The consequence is that weaker subjets are thrown away during trimming. The $k_t$ algorithm clusters radiation from to softest to hardest, this produces an equal allocation of energy amongst subjets that contain final state radiation, this increases their chance to be kept during trimming. The ATLAS standard values of $R_{sub}$ is 0.2 and for $f_{cut}$ is 5%. These values have been seen to improve pileup stability and increasing the large-R jet mass reconstruction [72].

## 3.3 The comparison of the fast and full simulation distributions

The comparison between the fast and full simulation is performed using large-R jet substructure variables to check if the variable reconstruction is identical. Any deviations of the fast simulation variables from the full simulation variables will be studied to make suggestions to the fast simulation developers. This is because full simulation describes real data best.

The large amounts of data collected at ATLAS in run-II motivated this study. Generally, the W′ searches are conducted using the full simulation, but now since amounts of data have increased, this means that comparable Monte-Carlo simulation is needed and it can only be achieved by faster simulations. Although the fast simulation also has its own disadvantages like reduced accuracy that may be accepted for some particles and sub-detector regions but not all [55]. The choice of the simulation to be used is then determined by individual analyses.

The signal samples that are used in this study are simulated using the PYTHIA8 [73] generator with the NNPDF2.3LO [74] parton distribution function (PDF), which is set in conjunction with the A14 tune [75]. They were then processed through the fast and full ATLAS detector simulation, with the Z′ mass at 5 TeV.

### 3.3.1 Large-R jet substructure variables

**Splitting Scales** The splitting scale variable takes advantage of the clustering history of the two-body heavy particle decay in order to probe their jet substructure [68]. The splitting scale is mathematically [76] described as:

$$\sqrt{d_{ij}} = \min(p_{Ti}, p_{Tj}) \times \Delta R_{ij} \quad \text{where} \quad \Delta R = \sqrt{\Delta\phi_{i,j}^2 + \Delta\eta_{i,j}^2} \tag{3.1}$$

where $\Delta R_{ij}$ is the distance between two subjets $i$ and $j$ in the $\eta - \phi$ space, where $\phi$ is the azimuthal scattering angle, $p_{Ti}$ and $p_{Tj}$ are the corresponding transverse momenta of the subjets.
These splitting scales are very sensitive to whether the last steps of the recombination corresponds to the merging of the decay products of massive particles. The re-clustering of the trimmed large-R jet with the $k_t$ algorithm determines the splitting scales [76].

**N-Subjettiness ($\tau_N$)** This is a variable that forces the constituents of a jet into substructure to observe how well do they fit with the hypothesis of N subjets, where N is the number of hard cores (prongs) in a jet. The axes within the jet are defined by the N subjets that are found by the $k_t$ clustering of the constituents of the trimmed large-R jet [77].
The N-subjettiness provides the opportunity to identify objects that are boosted by studying jets that have two or more components (known as lobes) of energy. The N-subjettiness has a straightforward measure of the energy flow properties. N-subjettiness allows the measure of how best jet energy aligns into subjets and is the true reference point in identifying boosted objects [77]. The ratio $\tau_N/\tau_{N-1}$ helps adjust the relative degree of the signal efficiency and background rejection. [77].

The transverse momentum ($p_T$) weighted sum of the distances of the constituents to the subjet axes defines the quantity $\tau_N$ [76]. Mathematically the $\tau_N$ is defined as follows:

$$\tau_N = \frac{1}{d_0} \sum_k p_{T,k} \min \{\Delta R_{1,k}, \Delta R_{2,k}, ..., \Delta R_{N,k}\} \quad \text{where} \quad d_0 = \sum_k p_{T,k} R_0 \tag{3.2}$$

In Equation 3.2 [77], $p_{T,k}$ is the transverse momentum of the constituent k, $\Delta R_{J,k} = \sqrt{(\eta_i - \eta_j)^2 + (\phi_i - \phi_j)^2}$ is the distance in the pseudo -rapidity-azimuthal plane between the J which is a subjet and k which is a constituent particle [76]. Finally $R_0$ is then defined as the characteristics jet radius that is used in the original jet clustering algorithm [77].

The 0, 1 and 2 number of prongs subjettiness are mathematically described as follows:

$$\tau_0(\beta) = \sum_{i \in J} p_{T_i} \Delta R^{\beta} \tag{3.3}$$

$$\tau_1(\beta) = \frac{1}{\tau_0(\beta)} \sum_{i \in J} p_{T_i} \Delta R^{\beta}_{a_{1,i}} \tag{3.4}$$

$$\tau_2(\beta) = \frac{1}{\tau_0(\beta)} \sum_{i \in J} p_{T_i} \min(\Delta R^{\beta}_{a_{1,i}}, \Delta R^{\beta}_{a_{2,i}}) \tag{3.5}$$

In Equation 3.3, Equation 3.4, Equation 3.5 [76], $\Delta R$ is the distance between the subjet i and the jet axis, $\beta$ is a parameter that is generally used to give weight to the angular separation of the jet constituents, in this study of $\beta = 1$ [76]. To calculate $\tau_N$ the definition of N axes is required, this ensures that the distance between each constituent and the axes is $R_{a_N,i}$. The summing is over all the constituents of the jet J, with the normalization of factor $\tau_0$ (Equation 3.3) equivalent to the magnitude of the $p_T$ that is multiplied by $\beta$ -exponential radius [77].

Two methods are used to describe the axis of a jet in the N-subjettiness variable, the first one takes into account the distance of all the jet constituents while the second method only chooses the axis of a jet to be in the direction of the jet constituent that has the high $p_T$ and this method is called the winner takes all (wta) [77]. The wta method uses the direction of the hardest constituent instead

of the subjet axis in the exclusive $k_t$, in such a way that the distance measure $\Delta R_{a1,i}$ is changing in the calculation [77].

The 2-prong subjettiness ($\tau_2^{wta}$) variable values are greater than the 3-prong subjettiness ($\tau_3^{wta}$) variable values, this is because N-subjettiness depends on the distance of the constituencies of the jet towards each other and the axis of the jet. The $\tau_{21}^{wta}$ and $\tau_{32}^{wta}$ are dimensionless variables that are generated by taking the ratio of the N-subjettiness functions that are found within the standard subjet axes and the wta axes. The ratio $\tau_{21}^{wta} \equiv \tau_2^{wta}/\tau_1^{wta}$ is used to separate the 2-prong structure of large-R jets which results from the hadronic decays of Z and W bosons from jets of light quarks and gluons, this is shown by Figure 3.4.

The discrimination between the large-R jets that are formed from top-quarks that decays hadronically, with very high transverse momentum, consists of a 3-prong subjet structure, which is provided by the ratio $\tau_{32}^{wta} \equiv \tau_3^{wta}/\tau_2^{wta}$ [76]. The main objective for $\tau_{32}^{wta}$ variable is to identify the top jets as jets with 3-prong subjet and non-top jets as jets with 2 or less prongs

**The energy correlation function (ECF)** The large-R jet ECF variable uses the information of the energies and pairwise angles of the particle within a jet. The ECF yields a very strong discrimination power comparable to other methods based on subjets. The N+1 point correlation functions are very sensitive to the N-prong substructure, given the angular exponent $\beta$ which can be continuously changed to optimize the discrimination power [78]. The 0-point, 1-point, 2 point, and 3-point energy correlation for a jet (J) are mathematically described by:

$$ECF(0, \beta) = 1 \tag{3.6}$$

$$ECF(1,\beta) = \sum_{i \in J} p_{Ti} \tag{3.7}$$

$$ECF(2,\beta) = \sum_{i<j \in J} p_{Ti} p_{Tj} (\Delta R_{ij})^{\beta} \tag{3.8}$$

$$ECF(3,\beta) = \sum_{i<j<k \in J} p_{Ti} p_{Tj} p_{Tk} (\Delta R_{ij} \Delta R_{ik} \Delta R_{jk})^{\beta} \tag{3.9}$$

In the above point energy correlation functions, the parameter $\beta$ gives the angular separation weight of the constituents, $R_{ij}$ is the Euclidean distance between $i$ and $j$ in the rapidity-azimuthal angle plane, where $R_{ij}^2 = (\eta_i - \eta_j)^2 + (\phi_i - \phi_j)^2$. The jet constituents $i$ is summed over the jet J [79].

### 3.3.2 Analysis strategy

To probe the large-R jet substructure observables the $Z' \to t\bar{t}$ high mass samples were used, where $t$ is the top quark and $\bar{t}$ is the anti-top quark. In most cases the $Z'$ samples provide the environment to study the top quark decaying hadronically, where the top quark is hypothesized to be one of the $W'$ decay daughter, hence there are similarities in the analysis strategy between these two searches. This allows us to use the $Z'$ samples and then apply the same techniques established to the $W'$ search. In the signal samples, the events were required to have at-least one large-R jet with transverse momentum that is greater than 350 GeV with $|\eta|$ less than 2, because the boosted top-quark jet with a radius equal to 1.0 is expected to have the minimum $p_T$ which is twice the mass of the particle it resulted from. The pseudo-rapidity cut is included because tracks are used during the calibration of jets, and these tracks are in this region.

### 3.3.3 Results

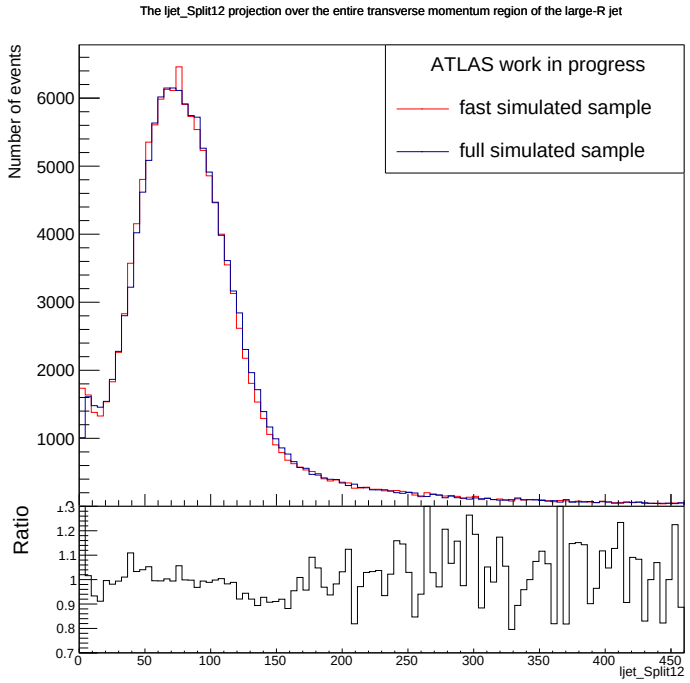



Figure 3.2: Shows the large-R jet first splitting scale variable distributions modelled by the fast and full simulation.

In this study of the hadronic top-quark, the expected value of the first splitting scale $\sqrt{d_{12}}$ of the fully captured decays in the large-R jet is approximated to be $m_t/2$, with $m_t$ is the mass of the top-quark. Fast simulation matches the full simulation with very minor mis-modelling of $\sqrt{d_{12}}$ as shown in Figure 3.2, where they both a peak at around 85 GeV which is approximately half of the top-quark mass. These minor deviations seem to occur at lower values of $\sqrt{d_{12}}$. The light quark or gluon jets tend to have mass approximately 20 GeV or less, with a very long tail that continues to the high $\sqrt{d_{12}}$. To distinguish heavy particle decays the parameter $\sqrt{d_{12}}$ is used, this parameter tends to be symmetric, but highly asymmetric in QCD splittings [68].

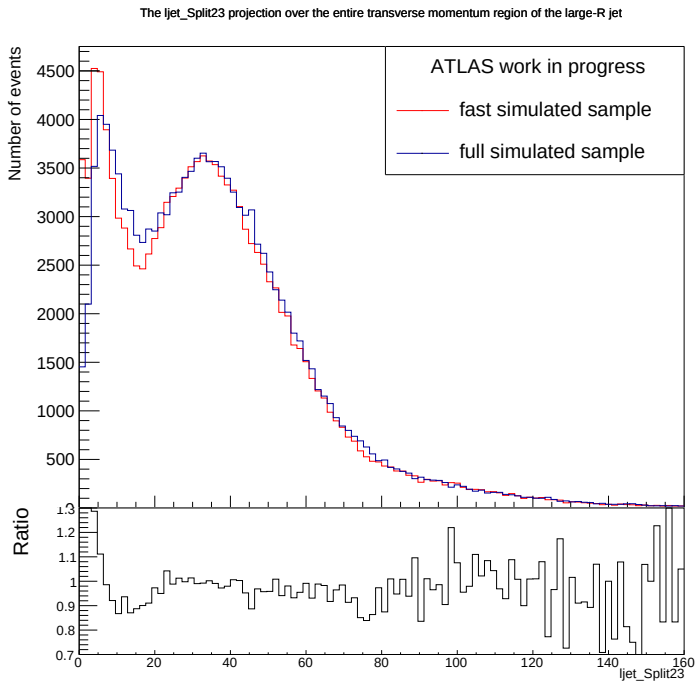



Figure 3.3: Shows the large-R jet second spitting scale variable distributions that is modelled by both the fast and full simulation.

The second splitting scale $\sqrt{d_{23}}$ value is approximated to be $m_W/2$ since it targets the hadronic decay of the W boson that decayed from the top-quark. In Figure 3.3 the fast simulation does not match the full simulation up to values around 35 GeV but thereafter then matches the full simulation. The peak of the second splitting scale around 40 GeV was also expected since this is half the mass of the W boson.

The fast simulation mis-models the $\tau_{21}^{wta}$ variable as shown by Figure 3.4 below, there are major differences compared to the full simulation. Fast simulation model tends to peak at lower values of $\tau_{21}^{wta}$ and never matches the full simulation. This fast simulation mis-modelling of the $\tau_{21}^{wta}$ can be attributed to the fewer clusters for the jet reconstruction that it uses.

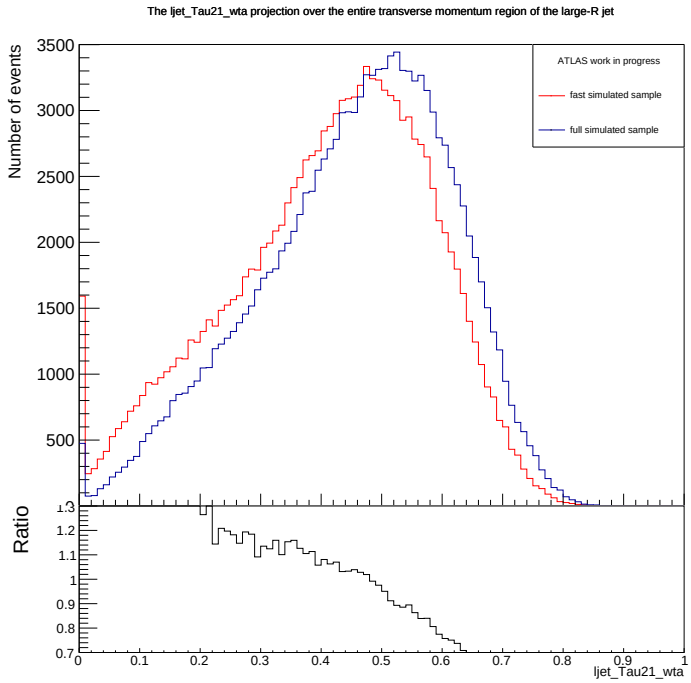



Figure 3.4: Shows the large-R jet $\tau_{21}^{wta}$ variable distributions modelled by the fast and full simulation.

Figure 3.5 clearly shows that the fast simulation fails to reconstruct the $\tau_{32}^{wta}$, this is observable as the fast simulation peaks at lower values of the $\tau_{32}^{wta}$. The use of fewer clusters by the fast simulation to reconstruct the variable $\tau_{32}^{wta}$ is the cause of this observed mis-modelling.

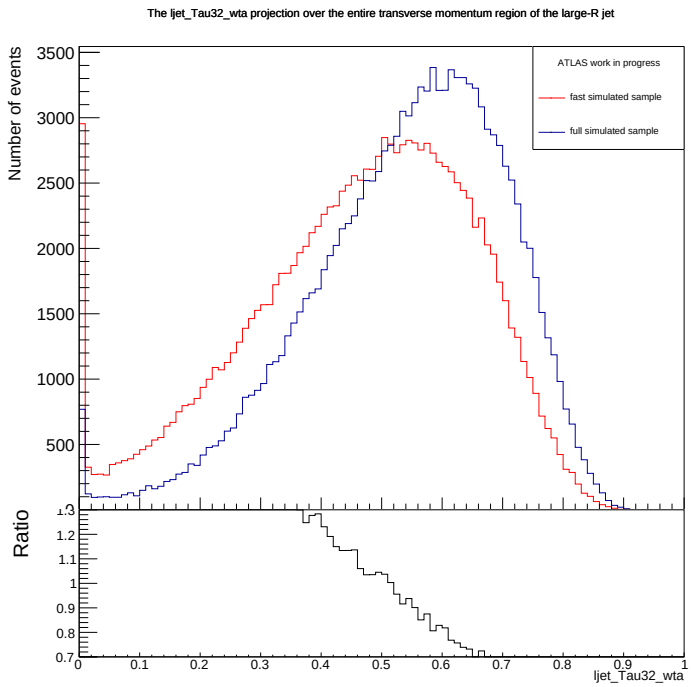
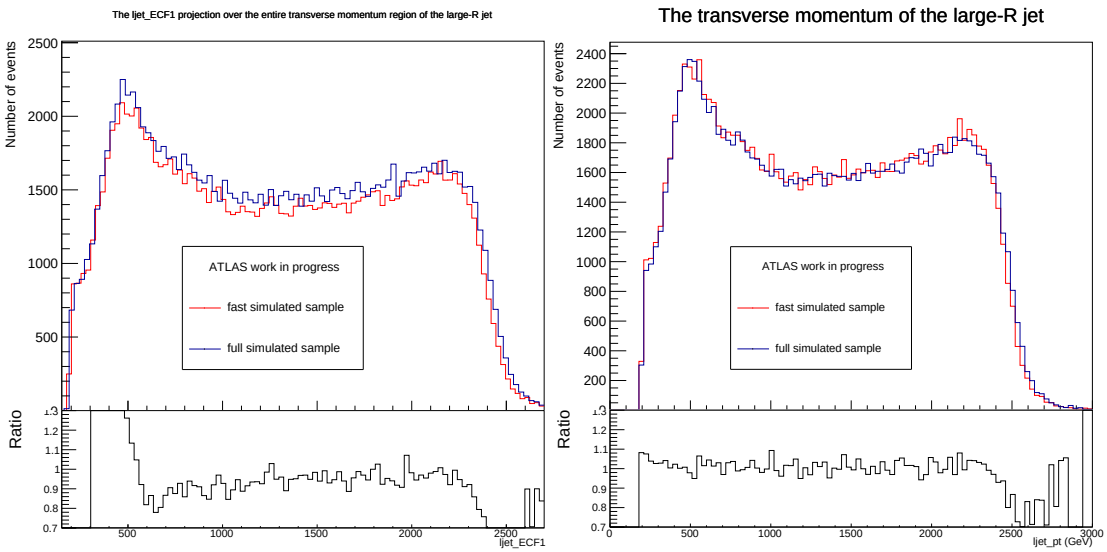



Figure 3.5: Shows the large-R jet $\tau_{32}^{wta}$ variable distributions modelled by the fast and match full simulation.

From Equation 3.7 the 1-point correlation shown by Figure 3.6a is approximately the large-R jet $p_T$ shown by Figure 3.6b. These distributions are indeed approximate even though there are some minor deviations at the lower end. This agreement between the ECF1 and the large-R jet $p_T$ shows that the event selection that was implemented in the signal sample leads to the results that are expected.

The $p_T$ of the large-R jet projection in Figure 3.6b, shows two peaks, the first peak is due to the contamination from QCD radiation at high $p_T$ and the second peak is of the large-R jet that results from the top-quark. The second peak around 2500 GeV was expected because it is assumed that the top-quark should have a $p_T$ that is half the mass of the Z′ boson.




(a) (b)

Figure 3.6: (a) Shows large-R jet ECF1 variable distributions that are modelled by the fast and full simulation. (b) Shows the large-R jet $p_T$ variable distributions modelled by fast and full simulation.

The 2-point correlation function is correlated to the particle mass that is undergoing the two-body decay in the coordinates of the collider [79] if $\beta$ is set to be 2 in Equation 3.8. In this case, the particle undergoing the two-body decay is the W boson and hence there is a peak around 80 GeV which is indeed the mass of the W boson, as it can be seen in Figure 3.7. In Figure 3.7 it is clear that the fast simulation peaks at approximately similar values as the full simulation but with more number of events. The fast simulation deviates from full simulation up to about 300 GeV but then matches it thereafter. The main reasons why the fast simulation deviated from the full simulation in this manner for the ECF2 and not deviated as it did to other jet substructure variables is not fully understood.
The ratios $ECF21 = ECF(2,\beta)/(ECF(1,\beta))^2$ and $ECF31 = ECF3(\beta)/(ECF(1,\beta))^3$ prove to be useful in identifying the two-body structure within the jet . ECF21 is specifically designed to define contours that separate 1-prong and 2-prong regions

of phase space. In doing so the ECF21 identifies the extent at which the jet is 1-prong or 2-prong in nature [80].

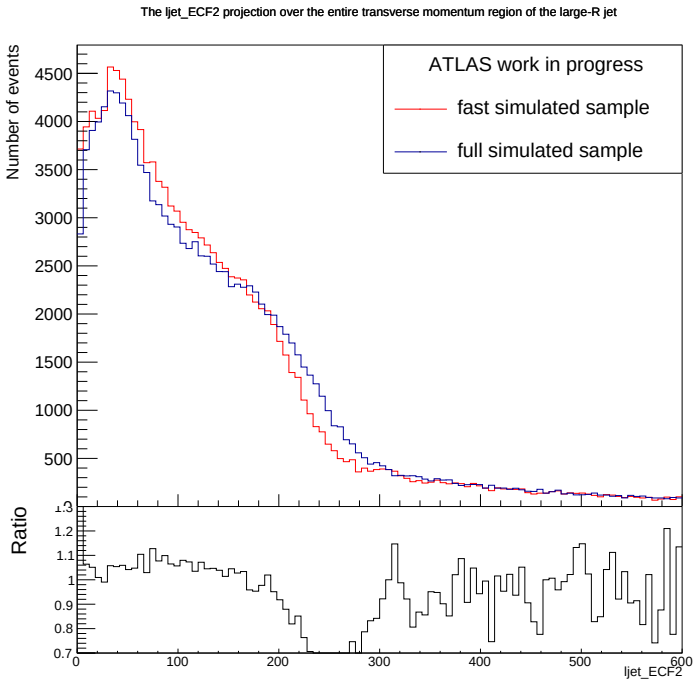



Figure 3.7: Shows the large-R jet 2-point correlation function variable distributions modelled by the fast and full simulation.

## 3.4 Summary of the fast and full simulation comparison

The use of the $Z'$ boson samples prove to be very insightful in this study of comparing the fast simulation with the full simulation using the jet substructure variables of the large-R jet. Fast simulation differs in modelling some of the large-R jet substructure variables compared to the full simulation. Major deviations can be seen on the $\tau_{21}^{wta}$, $\tau_{32}^{wta}$, and the ECF2 variables, as the fast simulation fails to match the full simulation. This is because, to reconstruct jets from the detec-

tor, the number of clusters that are used by simulation has an impact on how well the jet is reconstructed. The fast simulation uses a fewer number of clusters compared to the full simulation for its jet reconstruction in order to speed up the simulation time, this clearly leads to the jet substructure variables mentioned being reconstructed very poorly. This is evident since the fast simulated $\tau_{21}^{wta}$, $\tau_{32}^{wta}$, and the ECF2 variables peaks at lower values compared to the full simulation. The reconstruction of the splitting scale variables does not seem to be greatly affected even though the fast simulation deviates slightly from the full simulation at lower values but matches towards the peak and more or less thereafter. These deviations are not yet fully understood. The fast simulation splitting scale variable deviations to full simulation are not associated with the number of clusters that are used. The behaviour of these deviations is different from the ones observed in $\tau_{21}^{wta}$, $\tau_{32}^{wta}$, and the ECF2.

This study was repeated under different large-R jet $p_T$ regions to further probe the fast simulation deviations from the full simulation that have been observed. There was a suspicion that the fast simulation could be matching the full simulation in modelling the jet substructure under certain regions of the large-R jet $p_T$. The large-R jet $p_T$ was then divided into three regions: firstly from 0 to 500 GeV, from 500 to 1500 GeV, and lastly from 1500 GeV and above. The results of this study can be seen in Appendix A. Studying the jet substructure variables under these different large-R jet $p_T$ regions did not yield any new observation that had not been seen when scanning the entire spectrum of the large-R jet $p_T$.

## 3.5 Optimization of the top quark reconstruction

The search for the $W' \to tb$ in the fully hadronic channel is highly dependent on the reconstruction and identification of the top and bottom quarks, the daughters of the $W'$ boson [66]. They are identified using the jets that are reconstructed after their decay processes. These jets are generally denoted as top jets or top-quark jets and bottom jets or bottom quark jets referring to jets that arise from top quarks and bottom quarks respectively.

The top quark is reconstructed from its decays, the bottom quark and the SM W boson which further decays to two light quarks, as shown by Figure 3.1. Since quarks can not be observed in isolation, methods to identify these W′ boson daughters is essential.

The main objective of this study is to find the best pre-selection method that identifies the large-R jet that originates from the top quark using the signal sample. This will increase the sensitivity of the search for the W′ boson. This step is critical since light quarks and gluons can also give large-R jets which are considered as background.

Previously a similar study was performed to select the top jets candidates and the results were used by the ATLAS collaboration [66] with the W′ mass samples of 700 GeV and 1 TeV. In that study, 82% success rate was achieved. In this thesis, the studied W′ samples had a mass of 2, 3, 3.5, 4, and 5 TeV. This study aims to increase this current success rate by using methods or techniques that would also decrease the background significantly.

The signal samples that are used in this study are simulated using the PYTHIA8 generator with the NNPDF2.3LO parton distribution function (PDF), which is set in conjunction with the A14 tune. It is then processed through the full ATLAS

detector simulation.

### 3.5.1 Analysis approach

All the events that were studied are required to have at least one large-R jet with transverse momentum ($p_T$) above 500 GeV and mass above 40 GeV with $|\eta| > 2$. To ensure that the small-R jet(s) being used are indeed inside the large-R jet, the distance between the small-R jet and the large-R jet axis and this distance must be $\Delta R < 1$, since the large-R jet since has the radius of 1.0. All the large-R jets that meet the above requirements will further be probed by the methods that will be used.

### 3.5.2 Top-quark reconstruction methods

There are several approaches that were investigated in this study. The main goal of these methods is to select a top-quark jet candidate that will undergo the matching process described by subsection 3.5.3. These methods are:

**The mass combination (m_comb) method** This method combines the mass of the large-R jet $m_{ljet}$ and the mass of the small-R jet $m_{sjet}$ that has the highest $p_T$ (leading) which is inside the large-R jet concerned. The $m_{ljet}$ is varied by using the $\Delta$ parameter that takes values from 0.05 to 0.30 in the steps of 0.05. This parameter is scanned in order to determine its value that yields the highest matching fraction of selecting the top-quark candidate. This method is characterised by:

$$m_{comb} = m_{sjet} + \Delta * m_{ljet} \tag{3.10}$$

In an event, the large-R jet with the highest value of $m_{comb}$ is selected to be the

top-quark jet candidate.

**The modified m_comb method** This method varies both $m_{sjet}$ and the $m_{ljet}$ contributions simultaneously by using the parameter $\omega$ that takes values from 0.0 to 1.0 in the steps of 0.1 in order to determine the $\omega$ value that yields the highest matching fraction of selecting the top-quark jet candidate. This method is defined as follows :

$$m_{comb} = \omega * m_{sjet} + (1 - \omega) * m_{ljet} \tag{3.11}$$

$m_{comb}$ is a variable that is used to choose a large-R jet with the highest value to be the top-quark jet candidate.

**The deep neural network (DNN) top tagged method** This method uses the DNN trained variable for top tagging to select the top-quark jet candidate. This variable was trained, tested and validated by [81]. This method selects the top-quark jet candidate by checking if a given large-R jet in an event is tagged or not tagged, this is done by checking if for a large-R jet the DNN variable is equal to one if tagged or equal to zero if it is not tagged. If there is only one large-R jet that is tagged it will then be selected as the top jet candidate. If it happens that there is more than one large-R jet that is tagged, the $p_T$ of these tagged large-R jets is compared and the one with the highest $p_T$ is selected to be the top jet candidate. The events where there is no large-R jet that is tagged are discarded.

### 3.5.3 The matching process

In order to calculate the matching fraction of selecting the top-quark jet candidates in an event, the large-R jets that are chosen as top-quark jet candidates must be verified if they originated from the top-quark or not. This verification relies on the separation techniques that use truth information record which have the history of all the particles from the simulation program and the large-R jets selected at reconstruction level (reco level) that provides the conditions similar to the ones of the real data. The use of the truth objects will be distinguishable as they will always be referred to as truth (e.g large-R truth jet).

In order to verify if the top-quark jet candidate arises from the top-quark the following steps are performed:

- Check if $\Delta R$ distance between the top-quark jet candidate and the large-R truth jet at particle level is less than 0.75.
- If the above requirement is met, then the large-R truth jet will be checked if it originates arise from a top quark.
- This is done by calculating the distance $\Delta R$ between the large-R truth jet and the top-quark at parton level, if $\Delta R < 0.75$ the large-R truth jet is then considered to have arisen from the top quark.
- This conclusion implies that the large-R jet which is the top-jet candidate matches the top quark, then the matching process is complete.

To quantify how successful the method is in selecting true top-quark jets from top-quark candidates, the matching fraction is computed. In this case, the matching fraction is defined as the total number of events that contain true top-quark jets divided by the total number of events with a top-quark jet candidate.

## 3.6 Results

To make the matching-fraction distributions, the contents of each bin from the histogram that contain top-quark jets candidates that originated from the top-quark is divided by the contents of the corresponding bin from the histogram that contains top-quark jet candidates. These matching fraction values per bin will be used to construct the matching fraction distributions that will be shown below.

| $\Delta = 0.15$ | | | | | |
|---|---|---|---|---|---|
| $W'$ mass (TeV) | 2 | 3 | 3.5 | 4 | 5 |
| Total matching fraction | 0.869873 | 0.86335 | 0.850499 | 0.841594 | 0.823667 |

Table 3.1: Shows the total matching fraction for all the examined W′ mass samples, when $\Delta = 0.15$.

**The m_comb method** The use of the small-R jets inside a large-R jet concerned and the large-R jet mass in question as already described gives a good matching fraction that is consistent across the W′ mass samples as shown in Table 3.1.

The matching fraction was explored as a function of the large-R jet $p_T$ variable as shown by Figure 3.8, the main reason was to observe if the large-R jets top-quark candidates followed the trend of the top-quark $p_T$ distribution as it was expected. The jets that result from boosted objects are considered to be collimated, it is postulated that these jets are well reconstructed in small-R jets. The jets that result from non boosted objects are well separated and can be captured well in large-R jets. Hence, the use of small radii jets is advantageous at high $p_T$ and the use of large-R jets is favourable at low $p_T$.

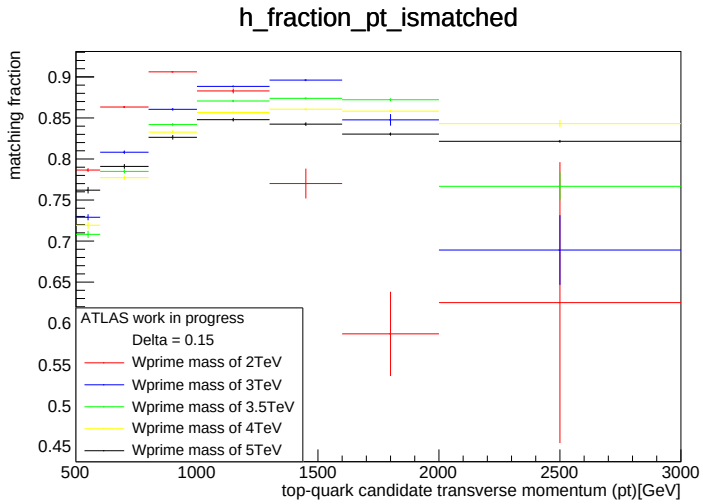



Figure 3.8: Shows the matching fraction when selecting the top-quark jet candidate under the large-R jet $p_T$ variable, for $\Delta = 0.15$.

It was expected that the transverse momentum of the top-quark candidates must be almost half the W′ mass, this is because from the two-body decay the daughters will have the momentum which is almost half the mass of the parent. This applies to the rest frame of reference. This means that if the W′ sample mass is 2 TeV one would expect to have a peak around 1 TeV for the transverse momentum of the top-quark jets, and this expectation was met, to confirm that the large-R jets top quark candidates that were chosen are top-quark jets.

The matching fraction was also explored as a function of the large-R jet top-quarks invariant mass variable as shown by Figure 3.9, to observe if the large-R jets top quark candidates had the mass of the top-quark mass which is about 173 GeV. Figure 3.9 shows that large-R jets with lower or higher masses compared to the top-quark are not likely to be selected as top-quark candidates, while large-R jets are mostly to be selected as top-quark candidates.

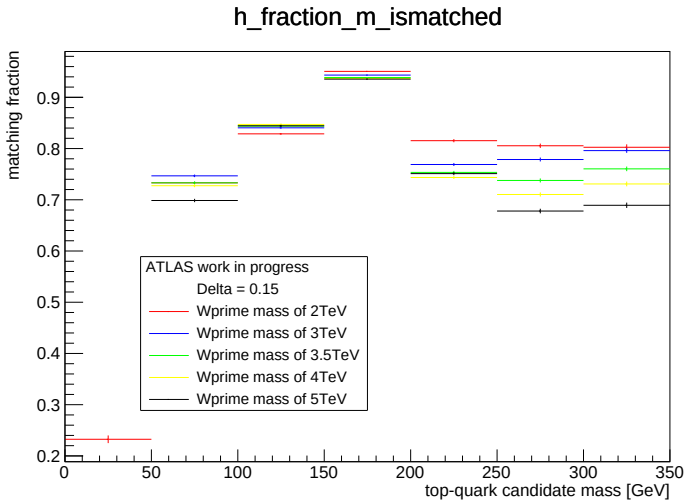



Figure 3.9: Shows the matching fraction for selecting the top-quark jet candidate using the large-R jet mass variable, when $\Delta = 0.15$.

**The modified m_comb method** The design of this method ensures that at $\omega = 0$ only the large-R jet mass is used for the top-quark candidates selection. At $\omega = 1$ it is only the mass of the small-R jets that are used in this selection. Table 3.2 shows that using large-R jets alone yields to a lower total matching fraction, it can be seen that the matching fraction decays from low to high W′ mass. This is expected since jets from boosted objects are assumed to be reconstructed well by small-R jets than large-R jets, implying that at lower W′ masses, the use of large-R jets alone will yield a better matching fraction.

| $\omega = 0$ | | | | | |
|---|---|---|---|---|---|
| $W'$ mass (TeV) | 2 | 3 | 3.5 | 4 | 5 |
| matching fraction | 0.805498 | 0.760274 | 0.740322 | 0.749294 | 0.717632 |

Table 3.2: Shows the total matching fraction for all the examined $W'$ mass samples for $\omega$ parameter equal to zero.

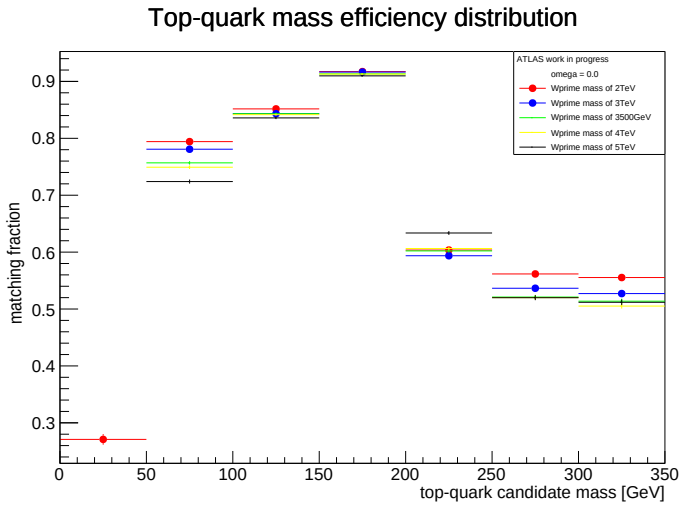



Figure 3.10: Shows the matching fraction for selecting the top-quark jet candidate under the large-R jet mass variable, when the parameter $\omega = 0$.

From Figure 3.10, it is clear that large-R jets with low or high masses compared to the top-quark mass are less likely to be selected to be top-quark candidates due to the lower matching fraction at this regions. This figure also shows that large-R jets with masses close to the top-quark mass are the most picked as top-quark candidates.

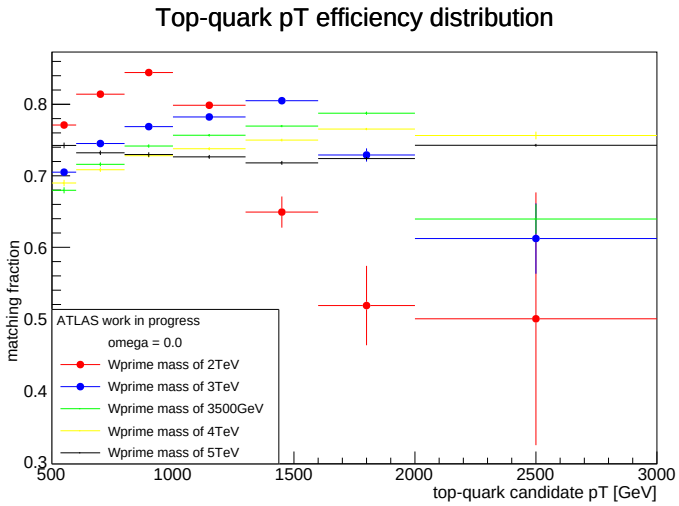



Figure 3.11: Shows the matching fraction for selecting the top-quark jet candidate using the large-R jet $p_T$ variable, when the parameter $\omega = 0$.

From Figure 3.11, it is clear that the selected large-R jet top-quark candidates $p_T$ has a peak around half the respective W′ masses, this shows with great confidence that the large-R top-quark jets resulted from the respective by W′, as this is how their $p_T$ is expected to be from the theory. This figure also shows that this method correctly selects more of the large-R jets that have a $p_T$ closer to the one expected (half the respective W′ masses) to be top jet candidates, this is evident since the matching fraction at these $p_T$ regions is highest.

| $\omega = 1$ | | | | | |
|---|---|---|---|---|---|
| $W'$ mass (TeV) | 2 | 3 | 3.5 | 4 | 5 |
| matching fraction | 0.857905 | 0.861096 | 0.853168 | 0.846362 | 0.831938 |

Table 3.3: Shows the total matching fraction for all the examined W′ mass samples, when $\omega = 1$.

When $\omega = 1$, by design there is only contribution from the small-R jet to select the top-quark jet candidates. Table 3.3 shows the consistent matching fraction across all the W′ mass samples.

In Figure 3.12, it is clear that the matching fraction begins at low values and increases until the half of the W′ mass for the respective samples, and decreases thereafter to very low values as the top jet candidates transverse momentum increased. This shows that more of the selected top jet candidates had the expected $p_T$, which is around half the respective W′ masses according to the two-body decay theory.

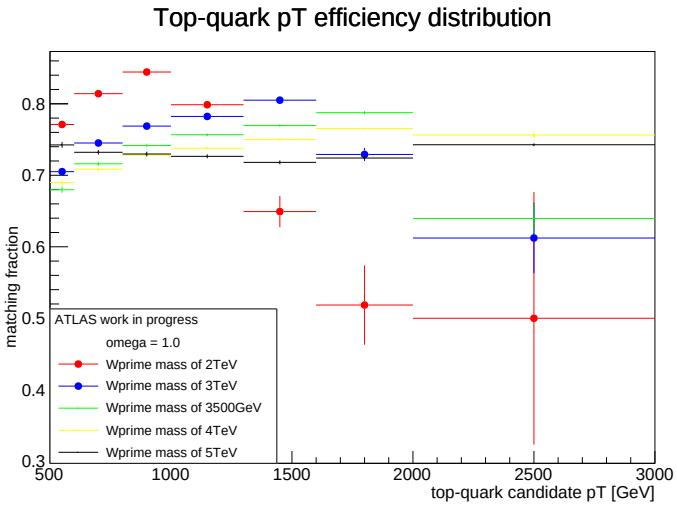



Figure 3.12: Shows the matching fraction when selecting the top-quark jet candidate using the large-R jet $p_T$ variable, for the parameter $\omega = 1$

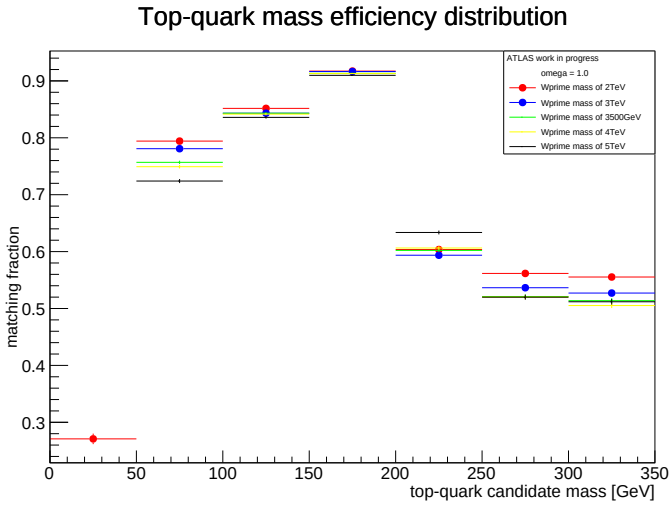



Figure 3.13: Shows the matching fraction when selecting the top-quark jet candidate under the large-R jet mass variable, for the parameter $\omega = 1$

In Figure 3.13, the matching fraction starts at very low values and increases as the mass of the top jet candidates grew towards the mass of the top-quark, where it is maximum, and then decreases drastically to very low values as the top jet candidates mass kept increasing. This demonstrates that large-R jets that have a mass close to the top-quark would be most likely to be selected as top jet

candidates.

| Top-quark is tagged | | | | | |
|---|---|---|---|---|---|
| $W'$ mass (TeV) | 2 | 3 | 3.5 | 4 | 5 |
| Total matching fraction | 0.935136 | 0.931024 | 0.928177 | 0.926777 | 0.924084 |

Table 3.4: Shows the total matching fraction for all the examined W′ mass samples using the dnn top tagging.

**The deep neural network (DNN) top tagged method** In Table 3.4, it is clear that the DNN top tagged variable shows a very high success rate of selecting the top-quark jet candidates that are true top-quark jets, with a total matching fraction of about 93%.

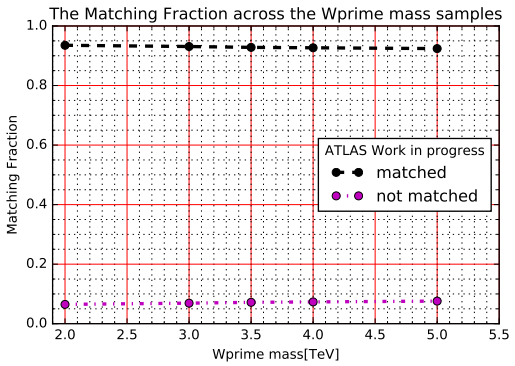



Figure 3.14: Shows the trend of total matching fraction for each W′ mass samples in selecting the true top-quark jets. Also shown is the fraction of discarding true top-quark jets for each W′ mass samples. Using the DNN top-quark tagging variable. The term 'matched' in the legend refers to the top jet candidates that matches the top quark, and the term 'not matched' refers to the top jets candidates that did not match the top quark

In Figure 3.14, the total matching fraction across all the W′ masses is very consistent. This shows that the DNN top tagged variable selects top jets candidates with a high chance that those are truly top jets. Figure 3.14 also shows the

agreement in its selection of top jet candidates, where the percentages of those that are true top jets and those that are not true top jets, sum up to be 100%.

Figure 3.15 was made using the 80% working point (WP80) of the DNN tagging variable which is a cut that allows 80% of the signal events to pass. This distribution is made to confirm if indeed this cut allowed 80% of the signal events, Figure 3.15 demonstrates that this variable does satisfy the expectation.

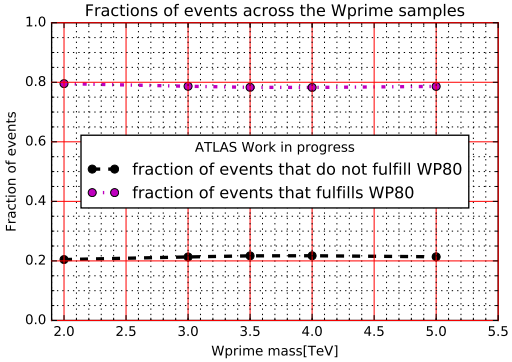



Figure 3.15: Shows the total fraction of events that fulfill the DNN top-quark tagger and the total fraction of events that do not fulfill the DNN top tagger at 80% working point.

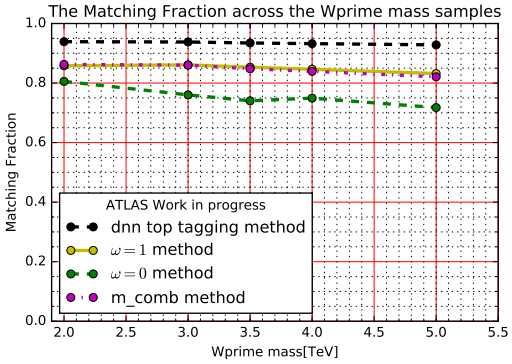



Figure 3.16: Shows the performance of all the methods studied across the W′ mass signal samples, where m_comb method uses $\Delta = 0.15$.

Figure 3.16, is a representation of all the methods that were studied for improvements in the top-quark reconstruction. It is evident that the DNN top tagging

method is superior amongst these methods, and using m_comb method with $\omega = 0$ yields the lowest total matching fraction across all the W′ masses. Using m_comb method with $\Delta = 0.15$ and the modified m_comb method with $\omega = 1$ produces a similar total matching fraction across the W′ masses. This relation is attributed to the fact that the m_comb method is dominated by the use of small-R jet mass inside the large-R jet and only 15% of the concerned large-R jet mass, while for the modified m_comb method with $\omega = 1$ it is only the mass of the small-R jets.

## 3.7 Optimization of the top-quark reconstruction summary

The use of the DNN method proved to be very significant to make this study as it produced the highest matching fraction in selecting the top-quark jet candidates. As it has already been shown by Table 3.4 for the 2 TeV W′ mass sample the total matching fraction reaches 94%, while in this method the lowest total matching fraction is 92% for the 5 TeV W′ mass sample.

After studying the m_comb method results, there was a motivation to modify it in order to achieve better results. Since the m_comb method took into consideration of only the leading small-R jets, there was an attempt to perhaps vary this contribution while simultaneously changing the large-R jet contributions. This was the motivation for characterizing the modified m_comb method.

The scanning of the parameter $\omega$ proved helpful in understanding the role of small-R jets and large-R jets in selecting the large-R jet top-quark candidates. Even though this method did not provide significant improvements on the matching fraction but it provided us with new ideas. This is because when $\omega$ is zero we have the full contribution of the large-R jet and from Table 3.2 it is clear that the total matching fraction is very low. When the $\omega$ parameter is one, which means

that there was an only small-R jet contribution in the method, as Table 3.3 shows the total fraction to be high even though still comparing to the matching fraction provided by the $\Delta = 0.15$ method, but after this method, it was clear that small-R jets had a significant contribution on selecting the large-R jet top-quark candidates.

# Chapter 4

# Conclusions

Studies on reconstruction and identification of a hypothetical heavy W′ particle was discussed in this thesis. The comparison of fast and full simulation samples shows that the jet substructure variables such as energy correlation functions and N-subjettiness depend on the number of clusters that these two simulations use for reconstruction. This is evident since the mentioned variables show major deviations which are linked to the use of fewer clusters in fast simulation compared to full simulations during reconstruction. This study demonstrated that these simulations are not in agreement in these variables while there is consensus in the splitting scales. This suggests that the fast simulation still needs improvements on its jet substructure variable reconstruction using clusters.

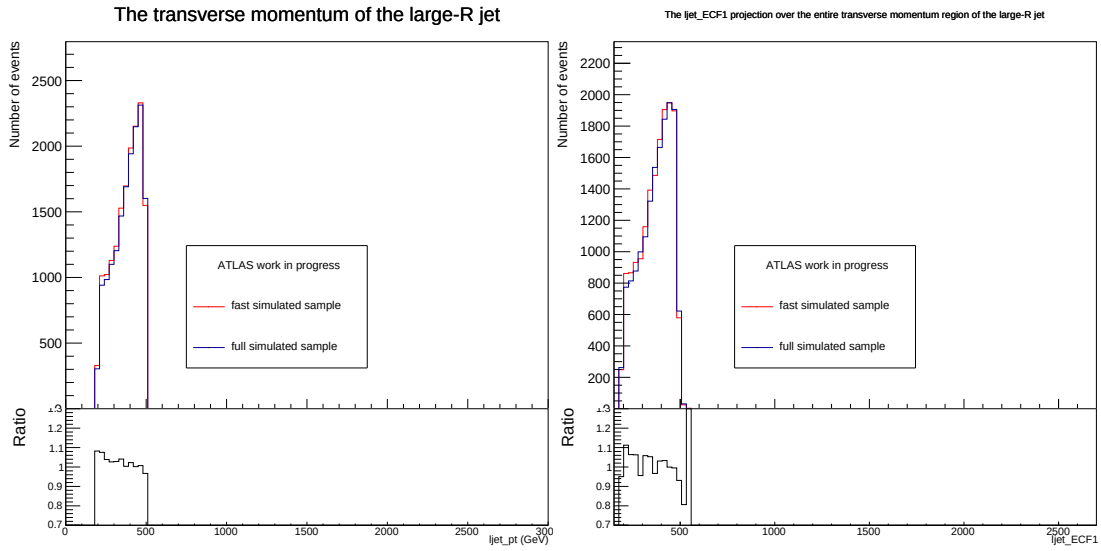
Figure 3.16 distributions show a comparison of the total matching fraction for all the methods that were studied, with the aim to optimize the selection of top quarks in the signal region. The total matching fraction produced by each method is shown in this distribution in comparison to other methods. The DNN top tagging method proves to be superior compared to all other methods. When $\omega = 0$ the selection of the top-quark candidates is at the lowest compared to other values of $\omega$, this indicates that the mass the large-R jet alone is not sufficient in the selection of the top quark jets. Although the mass of the small-R jets alone

seems to produce a better option for the selection of top quark jets, the m_comb method where $\Delta = 0.15$ is preferred since its matching fraction does not fall too much as a function of the signal mass samples. The DNN top tagging method will be used for the reconstruction of the top-quark in the future searches for the W$'$ boson.

# Appendix A

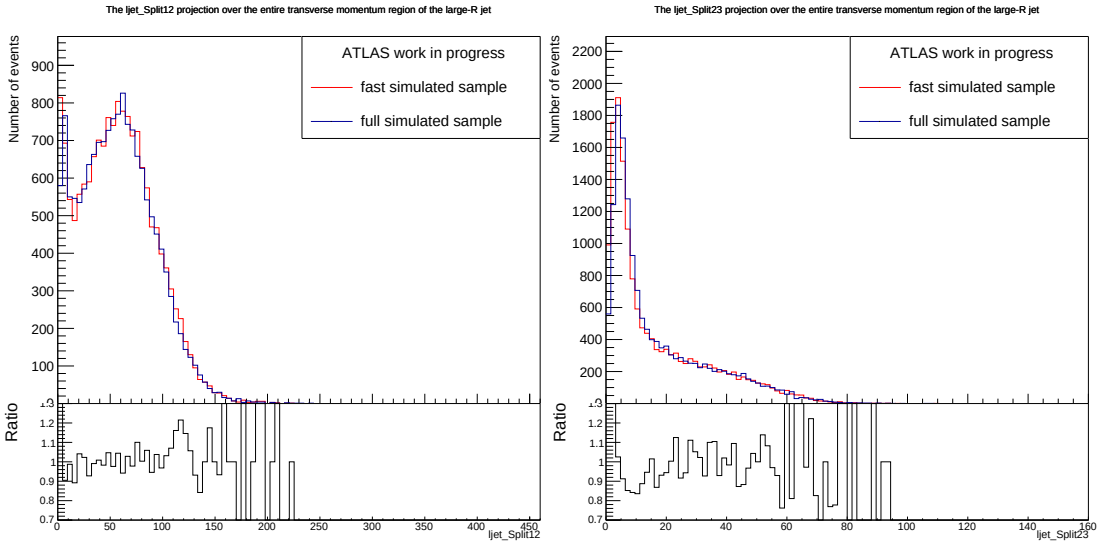
# Supporting distributions

**The distributions shown below represent were achieved using the second region (0 to 500 GeV) of the large-R jet $p_T$**



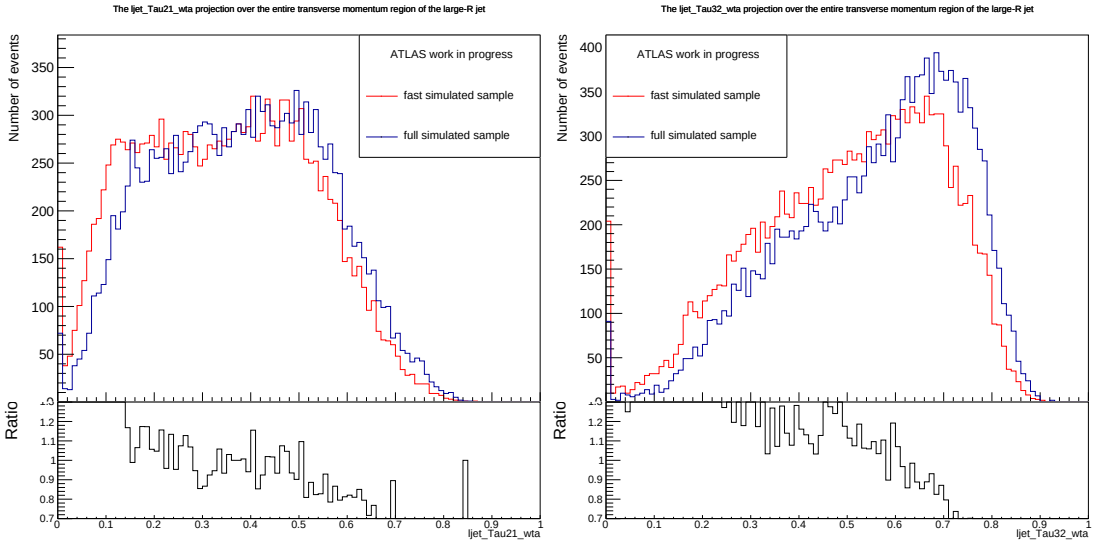

(a) (b)

Figure A.1: (a) Shows the large-R jet $p_T$ variable from 0 to 500 GeV modelled by the fast and full simulation. (b) Shows the 1-point correlation function variable distributions under the large-R jet $p_T$ region of 0 to 500 GeV, it is modelled by the fast and full simulation.




(a) (b)

Figure A.2: Shows (a) the first splitting scale and (b) the second splitting scale variable distributions under the large-R jet $p_T$ region of 0 to 500 GeV, it is modelled by the fast and full simulation.




(a) (b)

Figure A.3: Shows for (a) the $\tau_{21}^{wta}$ and (b) the $\tau_{32}^{wta}$ variable distributions under the large-R jet $p_T$ region of 0 to 500 GeV, modelled by the fast and full simulation.

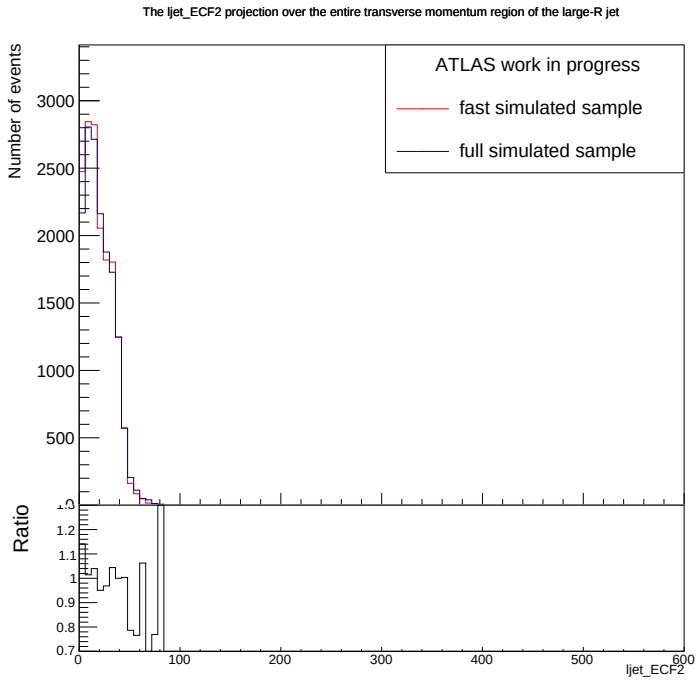
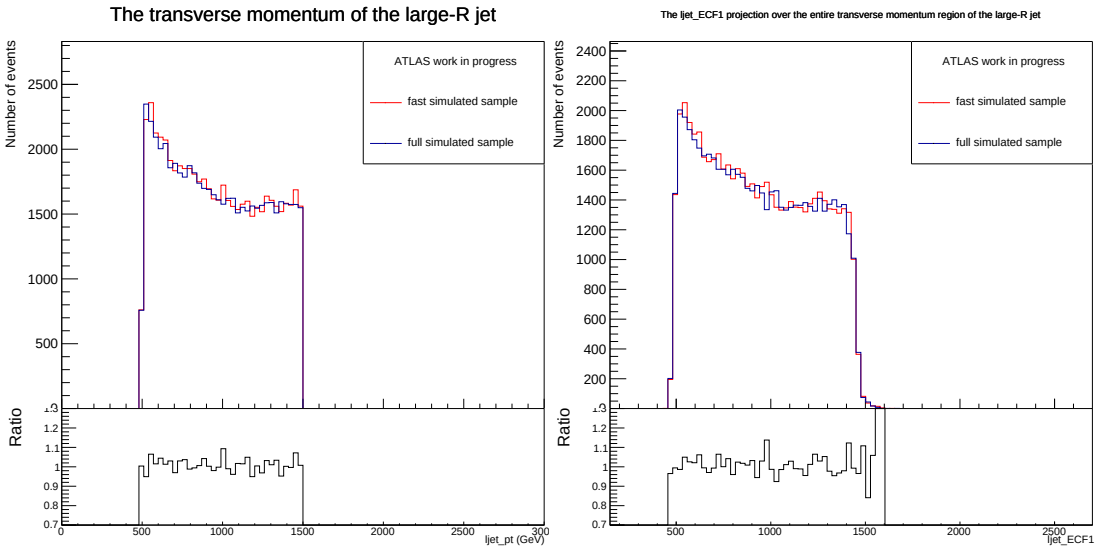


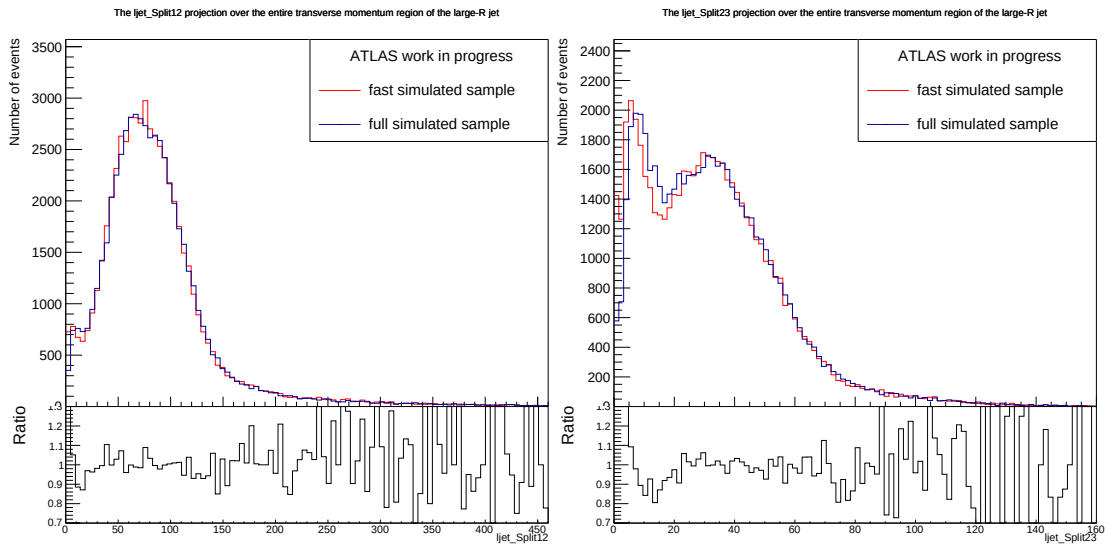

Figure A.4: Shows the 2-point correlation function variable distributions under the large-R jet $p_T$ region of 0 to 500 GeV, modelled by the fast and full simulation.

**The distributions shown below represent were achieved using the second region (500 to 1500 GeV) of the large-R jet $p_T$**



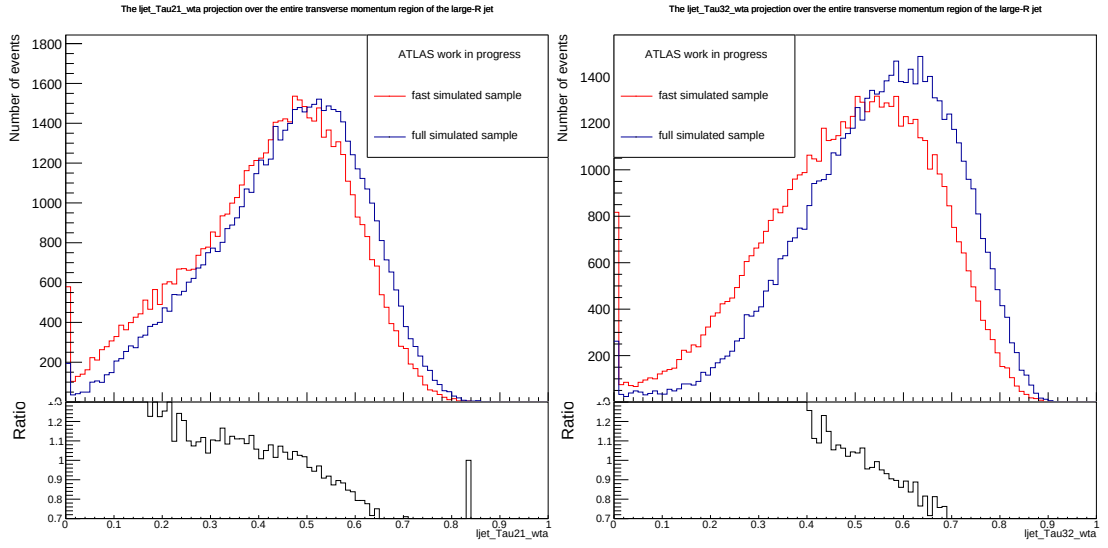

(a) (b)

Figure A.5: (a) Shows the large-R jet $p_T$ variable from 500 to 1500 GeV modelled by the fast and full simulation. (b) Shows the 1-point correlation function variable distributions under the large-R jet $p_T$ region of 500 to 1500 GeV, it is modelled by the fast and full simulation.




(a) (b)

Figure A.6: Shows (a) the first splitting scale and (b) the second splitting scale variable distributions under the large-R jet $p_T$ region of 500 to 1500 GeV, it is modelled by the fast and full simulation.




(a) (b)

Figure A.7: Shows for (a) the $\tau_{21}^{wta}$ and (b) the $\tau_{32}^{wta}$ variable distributions under the large-R jet $p_T$ region of 500 to 1500 GeV, modelled by the fast and full simulation.

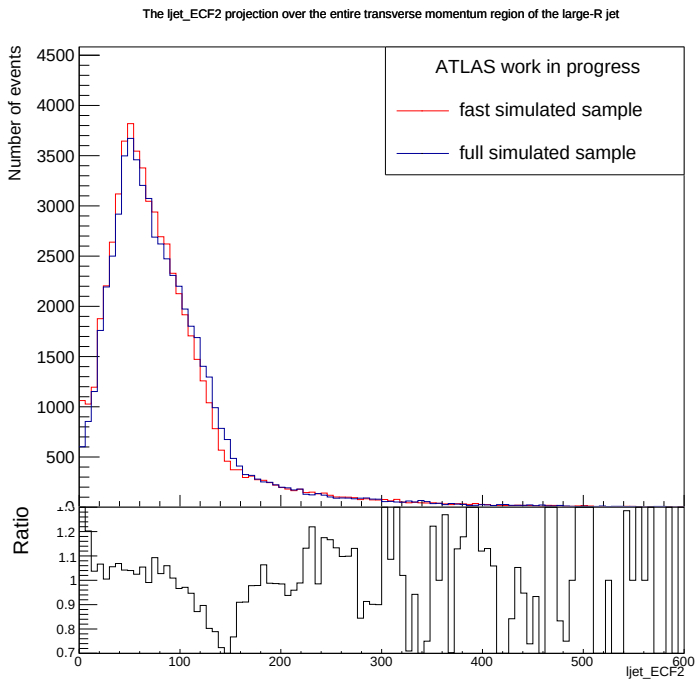
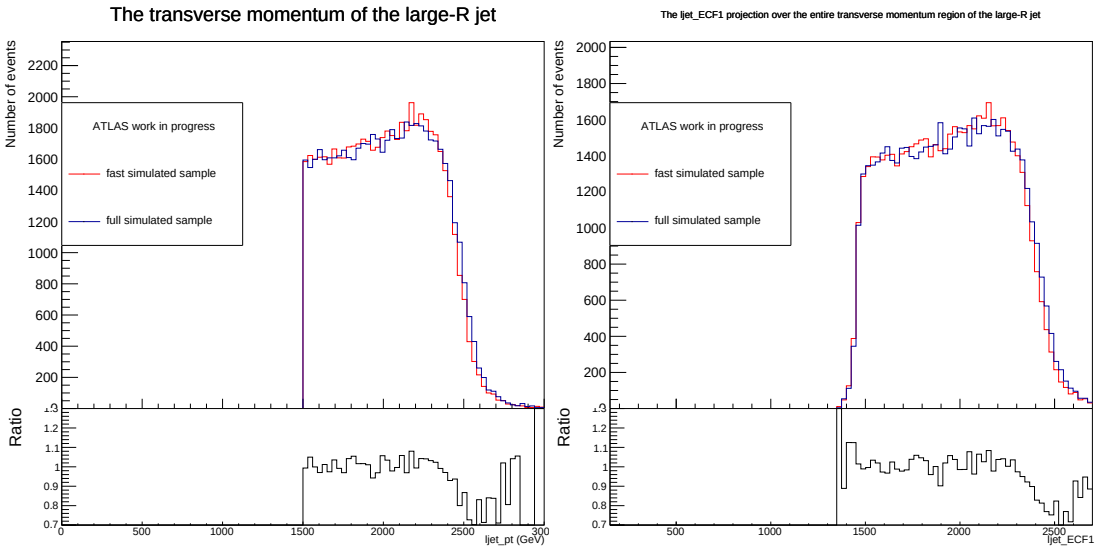


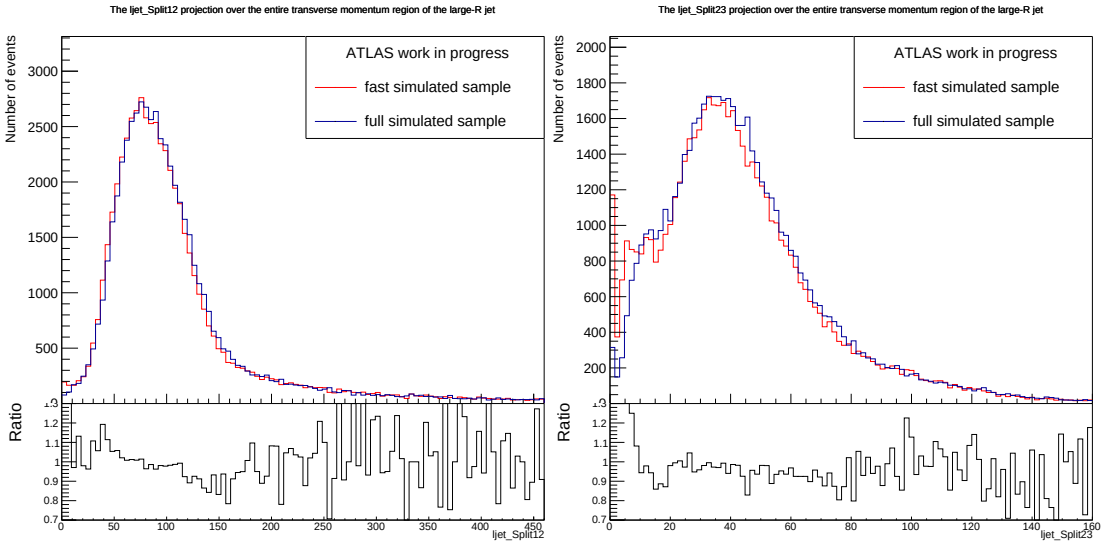

Figure A.8: Shows the 2-point correlation function variable distributions under the large-R jet $p_T$ region of 500 to 1500 GeV, modelled by the fast and full simulation.

**The distributions shown below represent were achieved using the last region (1500 GeV and above) of the large-R jet $p_T$**



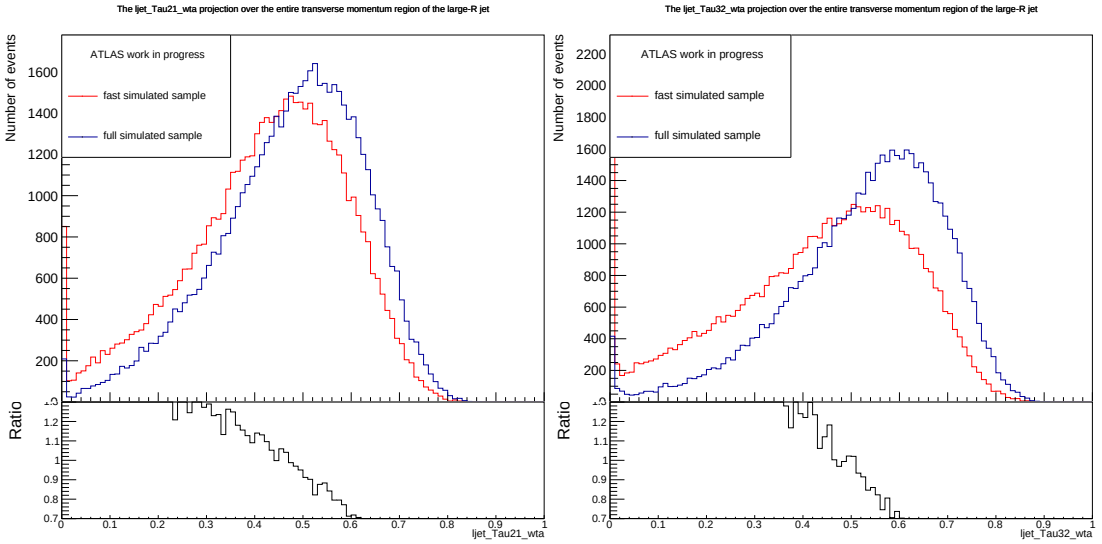

(a) (b)

Figure A.9: (a) Shows the large-R jet $p_T$ variable from 1500 GeV and above modelled by the fast and full simulation. (b) Shows the 1-point correlation function variable distributions under the large-R jet $p_T$ region of 1500 GeV and above, it is modelled by the fast and full simulation.




(a) (b)

Figure A.10: Shows (a) the first splitting scale and (b) the second splitting scale variable distributions under the large-R jet $p_T$ region of 1500 GeV and above, modelled by the fast and full simulation.




(a) (b)

Figure A.11: Shows for (a) the $\tau_{21}^{wta}$ and (b) the $\tau_{32}^{wta}$ variable distributions under the large-R jet $p_T$ region of 1500 GeV and above, modelled by the fast and full simulation.

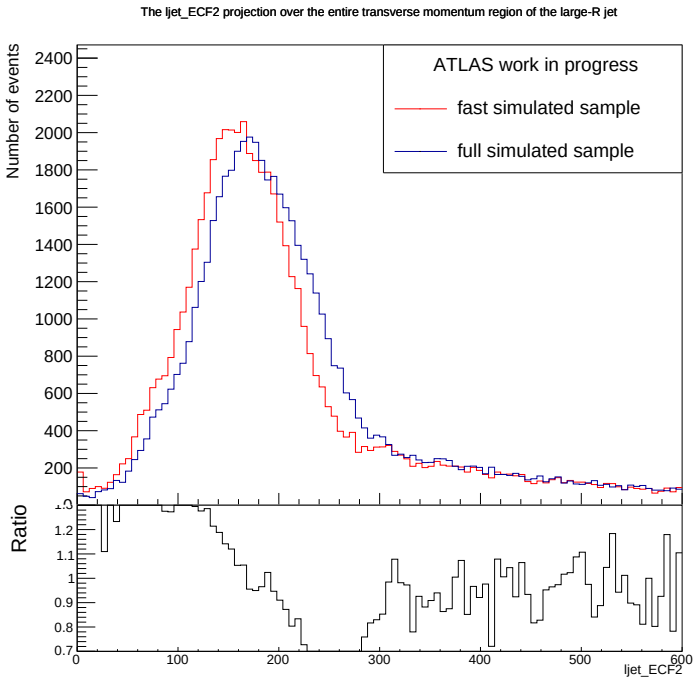



Figure A.12: Shows the 2-point correlation function variable distributions under the large-R jet $p_T$ region of 1500 GeV and above, as modelled by the fast and full simulation.

# References


[1] Hill, Edward L, "Hamilton's principle and the conservation theorems of mathematical physics," *Reviews of Modern Physics*, vol. 23, no. 3, p. 253, 1951. ix, 9

[2] E. Rutherford, "LXXIX. The scattering of $\alpha$ and $\beta$ particles by matter and the structure of the atom," *The London, Edinburgh, and Dublin Philosophical Magazine and Journal of Science*, vol. 21, no. 125, pp. 669–688, 1911. 1

[3] J. Chadwick, "Possible existence of a neutron," *Nature*, vol. 129, no. 3252, pp. 312–312, 1932. 1

[4] Thomson, Joseph John, "XL. Cathode rays," *The London, Edinburgh, and Dublin Philosophical Magazine and Journal of Science*, vol. 44, no. 269, pp. 293–316, 1897. 1

[5] M. Gell-Mann, "A schematic model of baryons and mesons," in *Murray Gell-Mann: Selected Papers*, pp. 151–152, World Scientific, 2010. 1

[6] ATLAS Collaboration, "Observation of a new particle in the search for the Standard Model Higgs boson with the ATLAS detector at the LHC," *Physics Letters B*, vol. 716, p. 129, Sep 2012. 1

[7] CMS collaboration, "A new boson with a mass of 125 GeV observed with

the CMS experiment at the Large Hadron Collider," *Science*, vol. 338, no. 6114, pp. 1569–1575, 2012. 1

[8] S. L. Glashow, "Partial-symmetries of weak interactions," *Nuclear Physics*, vol. 22, no. 4, pp. 579–588, 1961. 1, 7

[9] S. Weinberg, "WEINBERG 1967," *Phys. Rev. Lett*, vol. 19, p. 1264, 1967. 1

[10] Olive, Keith A, "Review of particle physics," *Chinese physics C*, vol. 38, no. 9, pp. 090001–090001, 2014. 1

[11] Halzen, Francis and Martin, Alan D, *Quark & Leptons: An Introductory Course In Modern Particle Physics*. John Wiley & Sons, 2008. 3, 6, 7, 8, 9, 10, 11

[12] A. R. Montalbano, *Search for the Standard Model Higgs boson produced with an associated W boson and decaying to a pair of b quarks at* $\sqrt{s} = 13$ *TeV with the ATLAS detector*. PhD thesis, Stony Brook U., 2017. 4

[13] C. Burgard, "Standard model of physics (2016)," *URL http://www. texample. net/tikz/examples/model-physics. Last viewed on May*, vol. 14, 2017. 5

[14] A. Jelinskas, *Search for heavy neutral MSSM Higgs bosons in the di-tau final state with the ATLAS detector*. PhD thesis, University of Warwick (GB), 2019. 5

[15] A. Salam, "Weak and electromagnetic interactions," *Elementary particle theory*, vol. 367, 1968. 7

[16] Aitchison, Ian JR and Aitchison, Ian Johnston Rhind, *An informal introduction to gauge field theories*. CUP Archive, 1982. 7

[17] H. D. Politzer, "Asymptotic freedom: An approach to strong interactions," *Physics Reports*, vol. 14, no. 4, pp. 129–180, 1974. 8

[18] F. Englert and R. Brout, "Broken symmetry and the mass of gauge vector mesons," *Physical Review Letters*, vol. 13, no. 9, p. 321, 1964. 10

[19] Higgs, Peter W, "Broken symmetries and the masses of gauge bosons," *Physical Review Letters*, vol. 13, no. 16, p. 508, 1964. 10

[20] A. Nisati and G. Tonelli, "The discovery of the Higgs boson at the Large Hadron Collider," *Riv. Nuovo Cim.*, vol. 38, pp. 507–573, 2015. 10

[21] G. Bertone, D. Hooper, and J. Silk, "Particle dark matter: Evidence, candidates and constraints," *Physics reports*, vol. 405, no. 5-6, pp. 279–390, 2005. 11

[22] D. B. Cline, "Sources of Dark Matter in the Universe: Proceedings of the 1st International Symposium," in *Sources of Dark Matter in the Universe: Proceedings of the 1st International Symposium*, pp. 1–336, World Scientific, 1995. 11

[23] W. De Blok, S. S. McGaugh, A. Bosma, and V. C. Rubin, "Mass density profiles of low surface brightness galaxies," *The Astrophysical Journal Letters*, vol. 552, no. 1, p. L23, 2001. 11

[24] D. Merritt, "Cosmology and convention," *Studies in History and Philosophy of Science Part B: Studies in History and Philosophy of Modern Physics*, vol. 57, pp. 41–52, 2017. 11

[25] A. G. Cohen, D. B. Kaplan, and A. E. Nelson, "Progress in electro-weak baryogenesis," *Annual Review of Nuclear and Particle Science*, vol. 43, no. 1, pp. 27–70, 1993. 11

[26] L. Canetti, M. Drewes, and M. Shaposhnikov, "Matter and Antimatter in the Universe," *New Journal of Physics*, vol. 14, no. 9, p. 095012, 2012. 11

[27] G. Altarelli, B. Mele, and M. Ruiz-Altaba, "Searching for new heavy vector bosons in p $\bar{p}$ colliders," *Zeitschrift für Physik C Particles and Fields*, vol. 45, no. 1, pp. 109–121, 1989. 12

[28] R. N. Mohapatra and J. C. Pati, "Natural left-right symmetry," *Physical Review D*, vol. 11, no. 9, p. 2558, 1975. 12, 34

[29] G. Senjanovic and R. N. Mohapatra, "Exact left-right symmetry and spontaneous violation of parity," *Physical Review D*, vol. 12, no. 5, p. 1502, 1975. 12, 34

[30] L. Rossi, "Superconductivity: its role, its success and its setbacks in the Large Hadron Collider of CERN," *Superconductor Science and Technology*, vol. 23, no. 3, p. 034001, 2010. 13

[31] C. A. Gottardo, "Search for charged lepton-flavour violation in top-quark decays at the LHC with the ATLAS detector," *arXiv preprint arXiv:1809.09048*, 2018. 13, 14, 15, 16, 17, 23

[32] ATLAS Collaboration, "The ATLAS experiment at the CERN large hadron collider," 2008. 13, 16, 18, 19, 20, 21, 23

[33] C. Kyungeon, *Search for a new heavy gauge boson in final states with one lepton and missing transverse momentum with the ATLAS detector.* PhD thesis, Indiana University Bloomington". 14

[34] E. A. Mobs, "The CERN accelerator complex. Complexe des acclrateurs du CERN," Oct 2016. General Photo. 15

[35] ATLAS Collaboration. https://twiki.cern.ch/twiki/pub/AtlasPublic/ApprovedPlotsDAQ/tdaq-run2-schematic2017.png. Accessed: 2019-07-25. 22

[36] R. Brun and F. Rademakers, "ROOTan object oriented data analysis framework," *Nuclear Instruments and Methods in Physics Research Section A: Accelerators, Spectrometers, Detectors and Associated Equipment*, vol. 389, no. 1-2, pp. 81–86, 1997. 23

[37] A. J. Larkoski, I. Moult, and B. Nachman, "Jet substructure at the large hadron collider: a review of recent advances in theory and machine learning," *arXiv preprint arXiv:1709.04464*, 2017. 23

[38] H. A. Andrews, L. Apolinario, R. A. Bertens, C. Bierlich, M. Cacciari, Y. Chen, Y.-T. Chien, L. C. Mendez, M. Deak, D. d'Enterria, *et al.*, "Novel tools and observables for jet physics in heavy-ion collisions," *arXiv preprint arXiv:1808.03689*, 2018. 25

[39] ATLAS Collaboration, "Topological cell clustering in the ATLAS calorimeters and its performance in lhc run," *Eur. Phys. J. C*, vol. 77, p. 490, 2017. 25

[40] ATLAS Collaboration, "ATLAS Jet Reconstruction, Calibration, and Tagging of Lorentz-boosted Objects," Tech. Rep. ATL-PHYS-PROC-2017-236, CERN, Geneva, Nov 2017. 25

[41] Schwartzman, Ariel, "Jet energy calibration at the LHC," *International Journal of Modern Physics A*, vol. 30, no. 31, p. 1546002, 2015. 26

[42] M. Aaboud *et al.*, "Jet energy scale measurements and their systematic uncertainties in proton-proton collisions at $\sqrt{s} = 13$ TeV with the ATLAS detector," *Phys. Rev. D*, vol. 96, p. 072002, Oct 2017. 27

[43] ATLAS Collaboration, "The ATLAS experiment at the CERN large hadron collider," *Jinst*, vol. 3, p. S08003, 2008. 27

[44] Z. Marshall, A. Rimoldi, R. Jones, J. Pilcher, T. Nunnemann, and D. Rousseau, "The ATLAS Simulation Infrastructure," 28, 29, 30, 31, 32

[45] M. Dobbs and J. B. Hansen, "The HepMC C++ Monte Carlo event record for high energy physics," *Computer Physics Communications*, vol. 134, no. 1, pp. 41–46, 2001. 28

[46] T. Sjöstrand, S. Mrenna, and P. Skands, "JHEP05 (2006) 026," *Comput. Phys. Comm*, vol. 178, p. 852, 2008. 28

[47] G. Corcella, I. G. Knowles, G. Marchesini, S. Moretti, K. Odagiri, P. Richardson, M. H. Seymour, and B. R. Webber, "HERWIG 6: an event generator for hadron emission reactions with interfering gluons (including supersymmetric processes)," *Journal of High Energy Physics*, vol. 2001, no. 01, p. 010, 2001. 28

[48] G. Corcella, I. G. Knowles, G. Marchesini, S. Moretti, K. Odagiri, P. Richardson, M. H. Seymour, and B. R. Webber, "HERWIG 6.5 release note," *arXiv preprint hep-ph/0210213*, 2002. 28

[49] G. Marchesini, B. R. Webber, G. Abbiendi, I. Knowles, M. H. Seymour, and L. Stanco, "HERWIG 5.1-a monte carlo event generator for simulating hadron emission reactions with interfering gluons," *Computer Physics Communications*, vol. 67, no. 3, pp. 465–508, 1992. 28

[50] T. Gleisberg, S. Hoeche, F. Krauss, A. Schälicke, S. Schumann, and J.-C. Winter, "SHERPA 1. $\alpha$, a proof-of-concept version," *Journal of High Energy Physics*, vol. 2004, no. 02, p. 056, 2004. 28

[51] S. Frixione, P. Nason, and B. R. Webber, "Matching NLO QCD and parton showers in heavy flavour production," *Journal of High Energy Physics*, vol. 2003, no. 08, p. 007, 2003. 28

[52] D. J. Lange, "The EvtGen particle decay simulation package," *Nuclear Instruments and Methods in Physics Research Section A: Accelerators, Spectrometers, Detectors and Associated Equipment*, vol. 462, no. 1-2, pp. 152–155, 2001. 28

[53] T. Stelzer and W. Long, "Automatic generation of tree level helicity amplitudes," *Computer Physics Communications*, vol. 81, no. 3, pp. 357–371, 1994. 28

[54] ATLAS Collaboration, "ATLAS computing: Technical design report," *LHCC Reports; ATLAS Techical Design Reports*, 2005. 28

[55] W. Lukas, "Fast simulation for ATLAS: Atlfast-II and ISF," in *Journal of Physics: Conference Series*, vol. 396, p. 022031, IOP Publishing, 2012. 29, 30, 31, 38

[56] T. Le Bleis, P. Klenze, "Physics Simulation with Geant4," p. 33, December 2014. 29

[57] A. Zaborowska, "Geant4 fast and full simulation for future circular collider studies," in *Journal of Physics: Conference Series*, vol. 898, p. 042053, IOP Publishing, 2017. 30, 31, 33

[58] ATLAS Collaboration, "GEANT4–a simulation toolkit," *Nucl. Instrum. Meth. A*, vol. 506, no. 25, p. 0, 2003. 30

[59] E. Barberio, J. Boudreau, B. Butler, S. Cheung, A. Dell'Acqua, A. di Simone, W. Ehrenfeld, M. Gallas, A. Glasow, E. Hughes, *et al.*, "The geant4-

based ATLAS fast electromagnetic shower simulation," in *Astroparticle, Particle And Space Physics, Detectors And Medical Physics Applications*, pp. 802–806, World Scientific, 2008. 31

[60] K. Edmonds, T. Lenz, J. Mechnich, S. Fleischmann, C. Magass, and A. Salzburger, "The fast ATLAS track simulation (FATRAS)," tech. rep., 2008. 32

[61] ATLAS Collaboration, "The simulation principle and performance of the ATLAS fast calorimeter simulation FastCaloSim," tech. rep., ATL-COM-PHYS-2010-838, 2010. 32

[62] ATLAS Collaboration, "Search for a new heavy gauge-boson resonance decaying into a lepton and missing transverse momentum in 36 $\text{fb}^{-1}$ of pp collisions at $\sqrt{s} = 13$ TeV with the ATLAS experiment," *The European Physical Journal C*, vol. 78, no. 5, p. 401, 2018. 34

[63] J. C. Pati and A. Salam, "Erratum: Lepton number as the fourth" color"," *Physical Review D*, vol. 11, no. 3, p. 703, 1975. 34

[64] M. Mitra, R. Ruiz, D. J. Scott, and M. Spannowsky, "Neutrino jets from high-mass w r gauge bosons in TeV-scale left-right symmetric models," *Physical Review D*, vol. 94, no. 9, p. 095016, 2016. 34

[65] A. M. Sirunyan, A. Tumasyan, W. Adam, F. Ambrogi, E. Asilar, T. Bergauer, J. Brandstetter, E. Brondolin, M. Dragicevic, J. Erö, *et al.*, "Search for heavy resonances decaying to a top quark and a bottom quark in the lepton+ jets final state in proton–proton collisions at 13 TeV," *Physics letters B*, vol. 777, pp. 39–63, 2018. 35

[66] ATLAS Collaboration, "Search for $W' \to tb$ decays in the hadronic final state using pp collisions at $\sqrt{s} = 13$ TeV with the ATLAS detector," *arXiv:1801.07893*, 2018. 35, 50

[67] J. M. Butterworth, J. R. Ellis, A. R. Raklev, and G. P. Salam, "Discovering baryon-number violating neutralino decays at the LHC," *Physical review letters*, vol. 103, no. 24, p. 241803, 2009. 35

[68] Miller, David W *et al.*, "Jet substructure in ATLAS," *arXiv preprint arXiv:1110.1094*, 2011. 35, 38, 43

[69] A. Altheimer, S. Arora, L. Asquith, G. Brooijmans, J. Butterworth, M. Campanelli, B. Chapleau, A. Cholakian, J. Chou, M. Dasgupta, *et al.*, "Jet Substructure at the Tevatron and LHC: New results, new tools, new benchmarks," *Journal of Physics G: Nuclear and Particle Physics*, vol. 39, no. 6, p. 063001, 2012. 35

[70] Z. Hall and J. Thaler, "Photon isolation and jet substructure," *Journal of High Energy Physics*, vol. 2018, no. 9, p. 164, 2018. 35

[71] M. Cacciari, G. P. Salam, and G. Soyez, "The anti-kt jet clustering algorithm," *Journal of High Energy Physics*, vol. 2008, no. 04, p. 063, 2008. 36

[72] D. Krohn, J. Thaler, and L.-T. Wang, "Jet trimming," *Journal of High Energy Physics*, vol. 2010, no. 2, p. 84, 2010. 37

[73] T. Sjöstrand, S. Mrenna, and P. Skands, "A brief introduction to PYTHIA 8.1," *Computer Physics Communications*, vol. 178, no. 11, pp. 852–867, 2008. 38

[74] R. D. Ball, V. Bertone, S. Carrazza, L. Del Debbio, S. Forte, A. Guffanti, N. P. Hartland, J. Rojo, N. Collaboration, *et al.*, "Parton distributions with QED corrections," *Nuclear Physics B*, vol. 877, no. 2, pp. 290–320, 2013. 38

[75] ATLAS Collaboration, "ATLAS PYTHIA 8 tunes to 7 TeV data.(2014)," tech. rep., ATL-PHYS-PUB-2014-021. https://cds. cern. ch/record/1966419. 38

[76] ATLAS Collaboration, "Identification of boosted, hadronically decaying W bosons and comparisons with ATLAS data taken at $\sqrt{s} = 8$ TeV," *The European Physical Journal C*, vol. 76, no. 3, p. 154, 2016. 38, 39, 40, 41

[77] J. Thaler and K. Van Tilburg, "Identifying boosted objects with N-subjettiness," *Journal of High Energy Physics*, vol. 2011, no. 3, p. 15, 2011. 39, 40, 41

[78] A. J. Larkoski, G. P. Salam, and J. Thaler, "Energy correlation functions for jet substructure," *Journal of High Energy Physics*, vol. 2013, no. 6, p. 108, 2013. 41

[79] Atlas Collaboration, "Identification of boosted, hadronically decaying W bosons and comparisons with ATLAS data taken at s= 8 TeV," 2016. 42, 47

[80] I. Moult, L. Necib, and J. Thaler, "New angles on energy correlation functions," *Journal of High Energy Physics*, vol. 2016, no. 12, p. 153, 2016. 48

[81] ATLAS Collaboration, "Performance of top-quark and

$W$

W-boson tagging with ATLAS in Run 2 of the LHC," *The European Physical Journal C*, vol. 79, Apr 2019. 52

[82] Asman, B and Rizvi, E and Landon, MPJ and Brawn, IP and Martin, TA and Keller, M and Hanke, P and Prieur, DPF and Schultz-Coulon, HC and Narayan, R and others, "The ATLAS level-1 calorimeter trigger: Preprocessor implementation and performance," *JINST*, vol. 7, p. P12008, 2012.

[83] J. Allison, "Facilities and methods: Geant4–a simulation toolkit," *Nuclear Physics News*, vol. 17, no. 2, pp. 20–24, 2007.

[84] R. L. Harrison, "Introduction to Monte Carlo simulation," in *AIP conference proceedings*, vol. 1204, pp. 17–21, AIP, 2010.

[85] M. Gyulassy and X.-N. Wang, "HIJING 1.0: a Monte Carlo program for parton and particle production in high energy hadronic and nuclear collisions," *Computer Physics Communications*, vol. 83, no. 2-3, pp. 307–331, 1994.

[86] M. L. Mangano, F. Piccinini, A. D. Polosa, M. Moretti, and R. Pittau, "ALPGEN, a generator for hard multiparton processes in hadronic collisions," *Journal of High Energy Physics*, vol. 2003, no. 07, p. 001, 2003.

[87] B. P. Kersevan and E. Richter-Was, "The Monte Carlo event generator AcerMC 2.0 with interfaces to PYTHIA 6.2 and HERWIG 6.5," *arXiv preprint hep-ph/0405247*, 2004.

[88] S. Jadach, J. H. Kühn, and Z. Was, "TAUOLA-a library of Monte Carlo programs to simulate decays of polarized $\tau$ leptons," *Computer Physics Communications*, vol. 64, no. 2, pp. 275–299, 1991.

[89] E. Barberio, B. van Eijk, and Z. Was, "PHOTOSa universal Monte Carlo for QED radiative corrections in decays," *Computer Physics Communications*, vol. 66, no. 1, pp. 115–128, 1991.

[90] F. E. Paige, S. D. Protopopescu, H. Baer, and X. Tata, "ISAJET 7.69: a Monte Carlo event generator for pp, pp and e+e- reactions," *arXiv preprint hep-ph/0312045*, vol. 26, 2003.

[91] M. Bähr, S. Gieseke, M. A. Gigg, D. Grellscheid, K. Hamilton, O. Latunde-Dada, S. Plätzer, P. Richardson, M. H. Seymour, A. Sherstnev, *et al.*, "Herwig++ physics and manual," *The European Physical Journal C*, vol. 58, no. 4, pp. 639–707, 2008.

[92] E. Boos, V. Bunichev, M. Dubinin, L. Dudko, V. Edneral, V. Ilyin, A. Kryukov, V. Savrin, A. Semenov, and A. Sherstnev, "CompHEP 4.4automatic computations from Lagrangians to events," *Nuclear Instruments and Methods in Physics Research Section A: Accelerators, Spectrometers, Detectors and Associated Equipment*, vol. 534, no. 1-2, pp. 250–259, 2004.

[93] A. Pukhov, E. Boos, M. Dubinin, V. Edneral, V. Ilyin, D. Kovalenko, A. Kryukov, V. Savrin, S. Shichanin, and A. Semenov, "CompHEP-a package for evaluation of Feynman diagrams and integration over multi-particle phase space. User's manual for version 33," *arXiv preprint hep-ph/9908288*, 1999.

[94] S. Agostinelli, J. Allison, K. a. Amako, J. Apostolakis, H. Araujo, P. Arce, M. Asai, D. Axen, S. Banerjee, G. Barrand, *et al.*, "GEANT4a simulation toolkit," *Nuclear instruments and methods in physics research section A: Accelerators, Spectrometers, Detectors and Associated Equipment*, vol. 506, no. 3, pp. 250–303, 2003.

[95] J. Allison, K. Amako, J. Apostolakis, H. Araujo, P. A. Dubois, M. Asai, G. Barrand, R. Capra, S. Chauvie, R. Chytracek, *et al.*, "Geant4 developments and applications," *IEEE Transactions on nuclear science*, vol. 53, no. 1, pp. 270–278, 2006.

[96] S. Armstrong, K. Assamagan, J. Baines, C. Bee, M. Biglietti, A. Bogaerts, V. Boisvert, M. Bosman, S. Brandt, B. Caron, *et al.*, "Architecture of the ATLAS high level trigger event selection software," *Nuclear Instruments and Methods in Physics Research Section A: Accelerators, Spectrometers, Detectors and Associated Equipment*, vol. 518, no. 1-2, pp. 537–541, 2004.

[97] V. Boisvert, P. Calafiura, G. Polesello, S. Rajagopalan, D. Rousseau, and S. George, "Final report of the ATLAS reconstruction task force," tech. rep., ATL-COM-SOFT-2003-012, 2003.

[98] E. Richter-Was, D. Froidevaux, and L. Poggioli, "ATLFAST 2.0 a fast simulation package for ATLAS," tech. rep., 1998.

[99] Z. Marshall *et al.*, "Validation and performance studies for the ATLAS simulation," in *Journal of Physics: Conference Series*, vol. 219, p. 032016, IOP Publishing, 2010.

[100] F. M. Turner, "Lucretius among the Victorians," *Victorian Studies*, vol. 16, no. 3, pp. 329–348, 1973.

[101] S. Kurz, *DESY: Search for Supersymmetry in Events with Jets and Missing Transverse Momentum with the CMS Experiment*. PhD thesis, DESY, 2018.

[102] J. F. Donoghue, "The effective field theory treatment of quantum gravity," in *AIP Conference Proceedings*, vol. 1483, pp. 73–94, AIP, 2012.

[103] R. N. Mohapatra and J. C. Pati, "Left-right gauge symmetry and an isoconjugate model of CP violation," *Physical Review D*, vol. 11, no. 3, p. 566, 1975.

[104] N. Arkani-Hamed, A. G. Cohen, E. Katz, and A. E. Nelson, "The littlest higgs," *Journal of High Energy Physics*, vol. 2002, no. 07, p. 034, 2002.

[105] M. J. Dugan, H. Georgi, and D. B. Kaplan, "Anatomy of a composite higgs model," *Nuclear Physics B*, vol. 254, pp. 299–326, 1985.

[106] K. Agashe, R. Contino, and A. Pomarol, "The minimal composite higgs model," *Nuclear Physics B*, vol. 719, no. 1-2, pp. 165–187, 2005.

[107] M. Abolins *et al.*, "The ATLAS data acquisition and high level trigger system," *Journal of Instrumentation*, vol. 11, 2016.

[108] ATLAS Collaboration, "Performance of the ATLAS trigger system in 2015," *Eur. Phys. J. C*, vol. 77, p. 317, 2017.

[109] W. P. Vazquez *et al.*, "The ATLAS data acquisition system: from run 1 to run 2," *Nuclear and particle physics proceedings*, vol. 273, pp. 939–944, 2016.

[110] N. Ilic, "The ATLAS Fast Tracker and Tracking at the High-Luminosity LHC," *Journal of Instrumentation*, vol. 12, no. 02, p. C02052, 2017.

[111] J. Huth *et al.*, "Toward a standardization of jet definitions, Conference Report (1990)," FERMILAB-CONF-90-249-E, Presented at Summer Study on High Energy Physics , 1990.